AFRL-VS-HA-TR-98-0069

STUDY OF SURFACE EFFECTS ON LG WAVE PROPAGATION IN HETEROGENEOUS CRUSTS BY A GS-BE HYBRID METHOD

R.S. Wu T. Lay
X.B. Xie L. Fu
S. Jin X.F. Chen

University of California/Santa Cruz
Institute of Tectonics
Santa Cruz, CA 95064

May 21, 1998

Final Report
1 Jan. 1995 to 31 Dec. 1997

DEPARTMENT OF ENERGY
Office of Non-Proliferation
and National Security
Washington, DC 20585

AIR FORCE RESEARCH LABORATORY
Space Vehicles Directorate
29 Randolph Road
AIR FORCE MATERIEL COMMAND
HANSCOM AFB, MA 01731-3010

SPONSORED BY
Department of Energy
Office of Non-Proliferation and National Security

MONITORED BY
Air Force Research Laboratory
CONTRACT No. F19628-95-K-0016

The views and conclusions contained in this document are those of the authors and should not be interpreted as representing the official policies, either express or implied, of the Air Force or U.S. Government.

This technical report has been reviewed and is approved for publication.

JAMES C. BATTIS
Contract Manager

CHARLES P. PIKE, Deputy Director
Integration and Operations Division

This report has been reviewed by the ESD Public Affairs Office (PA) and is releasable to the National Technical Information Service (NTIS).

Qualified requestors may obtain copies from the Defense Technical Information Center. All others should apply to the National Technical Information Service.

If your address has changed, or you wish to be removed from the mailing list, or if the addressee is no longer employed by your organization, please notify AFRL/VSOS-IM, 29 Randolph Road, Hanscom AFB, MA 01731-3010. This will assist us in maintaining a current mailing list.

Do not return copies of the report unless contractual obligations or notices on a specific document requires that it be returned.

REPORT DOCUMENTATION PAGE

Form Approved
OMB No. 074-0188

1. AGENCY USE ONLY (Leave blank)	2. REPORT DATE	3. REPORT TYPE AND DATES COVERED
	21 May 1998	Final, 1 Jan. 1995 to 31 Dec. 1997

4. TITLE AND SUBTITLE
Study of Surface Effects on Lg Wave Propagation in Heterogeneous Crusts by a GS-BE Hybrid Method

5. FUNDING NUMBERS
PE 69120H
PR DENN TA GM WU AS

Contract F19628-95-K-0016

6. AUTHOR(S)
R. S. Wu
X. B. Xie
S. Jin
T. Lay
L. Fu
X. F. Chen

7. PERFORMING ORGANIZATION NAME(S) AND ADDRESS(ES)
University of California/Santa Cruz
Institute of Tectonics
Santa Cruz, CA 95064

8. PERFORMING ORGANIZATION REPORT NUMBER

9. SPONSORING / MONITORING AGENCY NAME(S) AND ADDRESS(ES)
Air Force Research Laboratory
29 Randolph Road
Hanscom AFB, MA 01731-3010

Contract Manager: James Battis/VSBI

10. SPONSORING / MONITORING AGENCY REPORT NUMBER
AFRL-VS-HA-TR-98-0069

11. SUPPLEMENTARY NOTES
This research was sponsored by the Department of Energy, Office of Non-Proliferation and National Security, Washington, DC 20585

12a. DISTRIBUTION / AVAILABILITY STATEMENT
Approved for public release; distribution unlimited

12b. DISTRIBUTION CODE

13. ABSTRACT ***(Maximum 200 Words)***
The objective of this research is to study the effects of surface topography, near-surface (sedimentary) structure and the associated small-scale heterogeneities on regional wave propagation, which is critical for both discrimination and yield estimation in monitoring the Comprehensive Test Ban Treaty and the Nuclear Non-Proliferation Treaty. This subject is also relevant to determining crustal structures and static corrections in exploration seismology. Our aim is to develop a hybrid method which couples the recently developed fast screen propagator theory and methods (Wu, 1994; Wu and Xie, 1994; Wu and Huang, 1995) with Boundary Integral Equation (BIE) or Boundary Element (BE) methods to treat the influences of both volume heterogeneities and irregular interfaces, including the influence of surface topography. We test Chen's Global Generalized Reflection/Transmission Matrix method and the traditional boundary element method in our hybrid method. Connection formulations between the screen method and the BIE, BE methods have been developed and tested for the SH case. The excellent agreement between seismograms from direct propagation and from propagation using the connection formulas proves the correctness of the theory and the connection formulations. Numerical simulations of the influence of surface topography, sedimentary layers with rough bottoms, and small-scale random heterogeneities demonstrate the feasibility of the methodology. It is also shown that rough surface topography and an irregular sedimentary layer with scales close to the dominant wavelength can efficiently attenuate Lg waves.

14. SUBJECT TERMS
Seismic wave propagation
Lg wave
CTBT
Generalized screen method

15. NUMBER OF PAGES
62

16. PRICE CODE

17. SECURITY CLASSIFICATION OF REPORT	18. SECURITY CLASSIFICATION OF THIS PAGE	19. SECURITY CLASSIFICATION OF ABSTRACT	20. LIMITATION OF ABSTRACT
Unclassified	Unclassified	Unclassified	SAR

Contents

Illustrations

1 Introduction

The study of path effects of complex structure and heterogeneities on the excitation and propagation of regional phases in different areas remains critical for both discrimination and yield estimation procedures for monitoring the CTBT. The problem will be most severe in the case of Non-Proliferation monitoring, in which the potential nuclear tests may occur in very different geological and geophysical environments. Today, regional waves are one of the most important information sources for monitoring purpose. Due to the complexity involved in regional phase propagation, synthetic simulations will play an important role in areas where there is a lack of sufficient observations. To meet these requirements, the ultimate goal is to develop a computationally viable technique for calculating high-frequency (1 - 25 Hz) synthetic seismograms in regional distance ($>$ 1000 km) for three-dimensional, heterogeneous (on large and small scales) crustal structures including rough surface and interfaces.

In the past, boundary integral equation (BIE) or boundary element (BE) methods have been extensively used to study the effects of topography or sedimentary basin structures on ground motions at the surface. These have also been used to study the Lg blockage problem with limited success. Blockage is assumed to be caused by coastlines, mountains and sudden change of crustal thickness. However, numerical simulations of blockage by large-scale crustal structures have not succeeded in matching the observations (Campillo et al., 1993; Gibson and Campillo, 1994). Most simulations are either for surface topography or for irregular structure beneath a flat surface (sedimentary layer) due to the restriction of computational complexity. However, the combination of both surface-topography and sedimentary structure may have more dramatic influence. An irregular surface and low-velocity layer can both trap part of the Lg energy into the surface layer and scatter the Lg wave out of the crustal waveguide. Existing methods are also not capable of simulating the combined effects of both large-scale structure and the associated small-scale heterogeneities. Irregular topography and near-surface structure

are the manifestation of past and/or present tectonic processes which often produce crustal heterogeneities at different scales. The effects from the small-scale (wavelength-scale) heterogeneities must be taken into consideration in modeling blockage and other Lg propagation, scattering and attenuation phenomena.

Our aim is to develop a new hybrid numerical method by combining the generalized screen method with the boundary integral equation method. The generalized screen method can handle wave propagation in a heterogeneous waveguide with modest topography. The method is based on one-way wave equation theory (Wu, 1994; 1996; Wu and Xie, 1994; Wu and Huang, 1995). In the crustal waveguide environment, major wave energy is carried by forward propagating waves, including forward scattered waves, and therefore the neglect of backscattered waves in the modeling will not change the main features of regional phases in most cases. By neglecting backscattering in the theory, the method becomes a forward marching algorithm. The present value of the wavefield in a vertical cross-section in the waveguide can uniquely determine the wavefield in the next vertical cross-section. In this way, we can obtain the wavefield in successive vertical cross-sections throughout the entire waveguide. This method provide us with enormous savings in computing time and storage, and makes it a very efficient method which can propagate high frequency regional signals to very long distances.

Modest surface topography can be modeled by coordinate transformation in the generalized screen method. However, the algorithm for handling the topography is still in the process of development. On the other hand, the boundary integral equation and boundary element methods have the flexibility needed to incorporate complex topographic features into the model. However, since matrix operations are involved, the boundary integral equation method is not that efficient. When the ratio of model dimension to wavelength is too large, the computation time and memory requirement become formidable. This problem can be circumvented through a hybrid method. The hybrid method will combine the advantages of the above mentioned two methods and avoid their disadvantages. The Lg phases generated by the source are propagated to a certain distance with the generalized

screen method. Then, the output will be used as the input to boundary integral equation (BIE) or boundary element (BE) methods, and the later is used to calculate the interaction between the Lg wave and the complex waveguide structure with rough topographic features. This approach provides the ability to investigate the interaction between the Lg wave and crustal waveguides having complicated structures including severe topography for long distance propagation.

In this project, the screen method has been successfully developed for a crustal waveguide for 2-D SH-wave propagation. The boundary integral equation and boundary element methods and the corresponding connection schemes to the screen propagator have been developed and tested. Numerical examples demonstrated the feasibility of this hybrid approach. Preliminary numerical simulations on Lg propagation through complex waveguides with rough surface or rough bottom of sedimentary layers show interesting results.

2 Generalized Screen Method

For an isotropic 2D elastic medium, the SH and the P-SV waves are decoupled. Here, we treat only the SH problem to demonstrate the applicability of the screen propagators to a crustal waveguide. Under such a circumstance, the equation of motion becomes

$$-\omega^2\rho(\mathbf{r})u(\mathbf{r}) = \frac{\partial}{\partial x}[\mu(\mathbf{r})\frac{\partial}{\partial x}u] + \frac{\partial}{\partial z}[\mu(\mathbf{r})\frac{\partial}{\partial z}u] \tag{1}$$

where ω is the frequency, $\mathbf{r} = (x, z)$ is a 2D position vector, u is transverse displacement, ρ is the density of the medium, and μ is the shear rigidity. We decompose the parameters of the elastic medium and the total wave field into

$$\begin{aligned} \rho &= \rho_0 + \delta\rho \\ \mu &= \mu_0 + \delta\mu \\ u &= u^0 + U \end{aligned} \tag{2}$$

where ρ_0 and μ_0 are parameters of the background medium, $\delta\rho$ and $\delta\mu$ are corresponding perturbations, u^0 is the primary field and U is the scattered field. Then the SH wave equation can be rewritten as

$$\mu_0\nabla^2 U + \omega^2\rho_0 U = -[\omega^2\delta\rho u + \nabla\cdot\delta\mu\nabla u]\,, \tag{3}$$

or

$$(\nabla^2 + k^2)U(\mathbf{r}) = -k^2 F(\mathbf{r})u(\mathbf{r})\,, \tag{4}$$

where $k = \omega/v$ is the wavenumber in the background medium and v is the background S wave velocity defined by

$$v = \sqrt{\mu_0/\rho_0} \tag{5}$$

In the right-hand side of (4), $F(\mathbf{r})$ is a perturbation operator

$$F(\mathbf{r}) = \varepsilon_\rho(\mathbf{r}) + \frac{1}{k^2}\nabla\cdot\varepsilon_\mu\nabla\,, \tag{6}$$

with

$$\varepsilon_\rho(\mathbf{r}) = \frac{\delta\rho(\mathbf{r})}{\rho_0}\,, \tag{7}$$

$$\varepsilon_\mu(\mathbf{r}) = \frac{\delta\mu(\mathbf{r})}{\mu_0}\,. \tag{8}$$

Eq. (4) is a scalar Helmholtz equation. With a half-space scalar Green's function g^h, the scattered field U can be written as

$$U(\mathbf{r}_1) = k^2\int_V d^2\mathbf{r} g^h(\mathbf{r}_1;\mathbf{r})F(\mathbf{r})u(\mathbf{r})\,, \tag{9}$$

where the 2D integration is over the volume V including all the heterogeneities in the modeling space. Under the forward-scattering approximation, the total field and Green's function under the integration in the above equation can be replaced by their forward-scattering approximated counterparts, and the field can be calculated by a one-way marching algorithm along the x-direction using a dual domain technique.

2.1 Wide-Angle Screen Approximation

The half-space model can be sliced into thin-slabs perpendicular to the propagation direction. The weak scattering condition holds for each thin-slab. For each forward step, the forward-scattered field by the thin-slab is calculated and added to the primary field so that the updated field becomes the incident field for the next thin-slab. The formulas of the dual-domain implementation are summarized as follows:

$$U(x_1, K_z) = U_\rho(x_1, K_z) + U_\mu(x_1, K_z) \tag{10}$$

where

$$U_\rho(x_1, K_z) = ik \int_{x'}^{x_1} dx e^{i\gamma(x_1 - x)} \mathcal{C}[\frac{k}{\gamma} \varepsilon_\rho(z) u_0(z)] \tag{11}$$

$$U_\mu(x_1, K_z) = ik \int_{x'}^{x_1} dx e^{i\gamma(x_1 - x)} \left\{ \mathcal{C}[\varepsilon_\mu(z) \bar{\partial}_x u_0(z)] - i\mathcal{S}[\frac{K_z}{\gamma} \varepsilon_\mu(z) \bar{\partial}_z u_0(z)] \right\} \tag{12}$$

where $\mathcal{C}[f(z)]$ and $\mathcal{S}[f(z)]$ are the cosine and sine transforms, defined by

$$\begin{aligned} \mathcal{C}[f(z)] &= \int_0^\infty dz 2 \cos(K_z z) f(z) \\ \mathcal{S}[f(z)] &= \int_0^\infty dz 2 \sin(K_z z) f(z) \end{aligned} \tag{13}$$

In Eq. (11) and (12), u_0, $\bar{\partial}_x u_0$ and $\bar{\partial}_z u_0$ can be calculated by

$$\begin{aligned} u_0(x, z) &= \frac{1}{2\pi} \int_{-\infty}^\infty dK'_z e^{iK'_z z} e^{i\gamma'(x - x')} u_0(x', K'_z) \\ &= \mathcal{C}^{-1}[e^{i\gamma'(x - x')} u_0(x', K'_z)] \end{aligned} \tag{14}$$

and

$$\begin{aligned} \bar{\partial}_x u_0(x, z) &= \mathcal{C}^{-1}[e^{i\gamma'(x - x')} \frac{\gamma'}{k} u_0(x', K'_z)] \\ \bar{\partial}_z u_0(x, z) &= i\mathcal{S}^{-1}[e^{i\gamma'(x - x')} \frac{K'_z}{k} u_0(x', K'_z)] \end{aligned} \tag{15}$$

Eq. (11), (12), (14) and (15) are the dual-domain expressions of the wide-angle screen propagator for half-space SH problems.

The procedure can be summarized as follows.

1. Cosine transform the incident fields at the entrance of each thin-slab into the wavenumber domain.

2. Free propagate in the wavenumber domain and calculate the primary field and its gradient within the slab.

3. At each horizontal position within the slab, inverse cosine/sine transform the primary field and its gradients into the space domain and then interact with the medium perturbations ε_ρ and ε_μ.

4. Cosine/sine transform the distorted fields into the wavenumber domain and perform the divergence operations to get the scattered fields.

5. Calculate the primary field at the slab exit and add to the scattered field to form the total field as the incident field at the entrance of the next thin-slab.

6. Continue the procedure iteratively.

2.2 Small-Angle Screen Approximation and the Phase-Screen Propagator

When the energy of crustal guided waves is carried mainly by small-angle waves (with respect to the horizontal direction), small angle approximations can be invoked to simplify the theory and calculations. Under the phase-screen approximation, the heterogeneous half-space is represented by a series of half-screens embedded in the homogeneous background half-space. Waves propagate between screens in the wavenumber domain and interact with phase-screens in the space domain. The interaction is only a phase-delay operator (multiplication in space domain). The formula for dual-domain implementation is

$$\begin{aligned} u(x_1, K_z) &= u_0(x_1, K_z) + U(x_1, K_z) \\ &= e^{i\gamma(x_1 - x')} \int_0^\infty dz 2\cos(K_z z)[1 + ik2S_s(z)]u_0(x', z) \end{aligned}$$

$$\approx \quad e^{i\gamma(x_1-x')}\mathcal{C}\left[e^{2ikS_s(z)}u_0(x',z)\right] \tag{16}$$

where $exp[2ikS_s(z)]$ is the phase delay operator. The procedure can be summarized as follows.

1. Cosine transform the incident field at the starting plane into the wavenumber domain and free propagate to the screen.

2. Inverse cosine transform the incident field into the space domain and interact with the shear slowness screen (phase-screen) to get the transmitted field.

3. Cosine transform the transmitted field into the wavenumber domain and free propagate to the next screen.

4. Repeat the propagation and interaction screen-by-screen to the boundary of the model space.

2.3 Treatment of the Moho Discontinuity

The Moho discontinuity can be treated in two ways. One is to put the impedance boundary conditions in the formulation, the other is to treat the parameter changes as perturbations which are therefore incorporated into the screen interaction. The former has the advantage of computational efficiency. The latter has the flexibility of handling irregular interfaces. Here, we adopt the latter approach and check the validity of perturbation approach for the Moho discontinuity by a reflectivity method and a finite difference algorithm.

2.4 Numerical Tests for the Screen Method

In this section we give examples of using the half-space phase-screen algorithm for regional wave propagation. First, we show the accuracy of the method by comparing the synthetic seismograms generated by the screen method with those calculated by the reflectivity method. Shown in Figure 1 are synthetic seismograms for a simple one layer crust model (a 1D model) with a flat Moho discontinuity at the depth of 32 km. The source function is a Ricker wavelet with a dominant

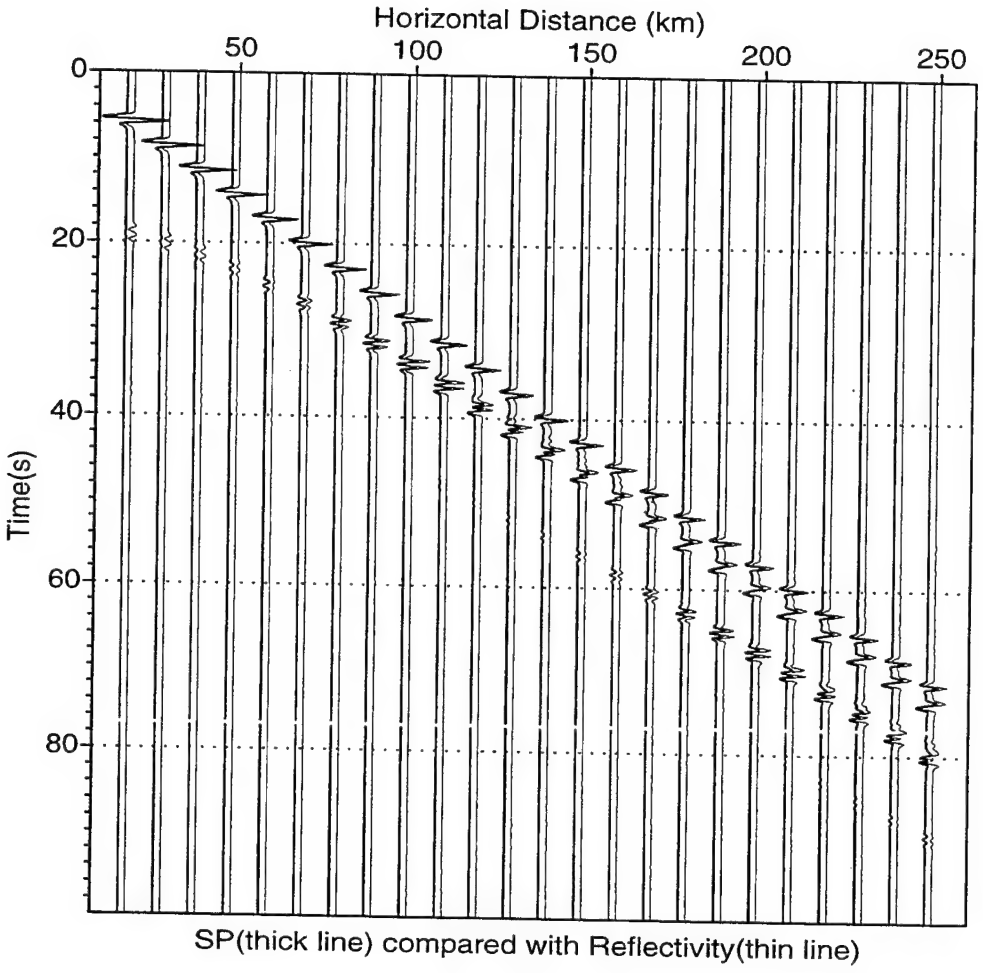

Figure 1: Comparison of synthetic seismograms along the surface calculated by the screen method and reflectivity method in wave-number domain. The model is a simple one layer crust model with a flat Moho discontinuity at the depth of 32 km. The source function is a Ricker wavelet with a dominant frequency of 1.0 Hz.

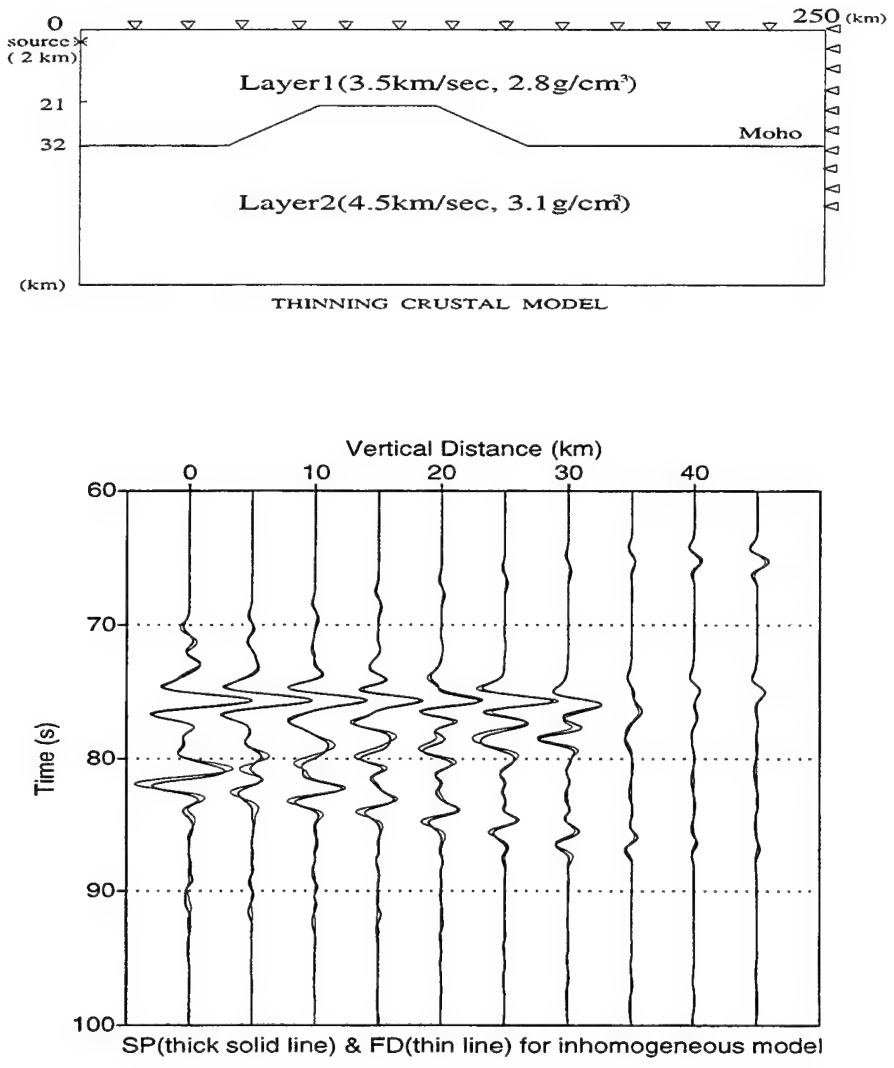

Figure 2: Comparison of synthetic seismograms along a vertical profile at a distance of 250 km calculated by the screen method and a finite-difference method. Shown in the upper panel is the crustal model and the lower panel shows synthetic seismograms. The thin lines are from the finite difference method and the thick lines are from the generalized screen method.

frequency of 1.0 Hz. Thin lines are from the reflectivity method and thick lines are from the generalized screen method. The source is located at a depth of 2 km, and its time function is a Ricker wavelet with a dominant frequency of 1.0 Hz. Except for near vertical reflections, where the one-way wave equation method fails, the results show excellent agreement. Then we show the accuracy of the method by comparing synthetic seismograms generated by this method with those generated by a finite difference algorithm (Xie and Lay, 1994). For the finite-difference method, a fourth-order elastic SH-wave code is used to calculate the synthetic seismograms. The spatial sampling interval is 0.25 km and the time interval is 0.025 *second*. For the screen method, the spatial sampling interval is 0.25 km in the vertical direction and the screen interval is 1.0 km. A Gaussian derivative is used as the source time function for both methods. Because of the computational intensity of the finite difference method, we did the comparison at short propagation distances. Shown on the top of Figure 2 is the crustal model used to calculate synthetic seismograms. The lower part shows the synthetic seismograms along a vertical profile at an epicenter distance of 250 km. The thin lines are from the finite difference method and the thick lines are from the generalized screen method. The source is located at a depth of 2 km. Excellent agreement can be seen.

Figure 3 shows the snap shots at 50 *sec.* for flat, necking and broadening crustal waveguides (from top to bottom, respectively) calculated using the screen method. The source is located at the top-left corner at depth 2 km. The development of the mantle wave and head wave, and the formation of crustal guided waves as multiple reflections between the free surface and Moho discontinuity can be clearly seen. For the inhomogeneous models, wave diffraction, leakage to the mantle, wavefront distortion and an increase of wavefield complexity can be seen clearly from the snapshots. It can be seen also that the passage through a narrow crustal segment has greater effect on Lg leakage than the passage through a broad segment. In the latter case, although the wavefronts are complicated due to scattering at the edges, most of the energy is still trapped in the crust, in contrast to the case of a narrow passage, in which a large percentage of energy leaks into the mantle. This example

demonstrates the potential of the screen method as a tool for investigating the path effects of different crustal structures.

The following example shows the potential capability of this method for long distance high-frequency wave propagation in a laterally varying structure. Figure 4 shows the laterally varying crustal model used in the calculation. Figure 5 shows the high-frequency synthetic seismograms on the surface at distances up to 1000 km for an inhomogeneous crustal waveguide. The center frequency is 5 Hz and the maximum frequency is 10 Hz. Shown in the right panel are synthetics at short distances (up to 500 km); on the left panel are synthetics for long distances (up to 1000 km). In this case, the Lg group is formed by multiple reflections by the Moho and the crustal discontinuities. This example demonstrates the potential capability of the generalized screen methods. In comparison, the low-frequency (f_c = 1 Hz, f_{max} = 2 Hz) synthetic seismograms are shown in Figure 6. It is clear that without high-frequency content, many of the distinctive features associated with the Lg measurements cannot be adequately modeled.

2.5 The Influence of Random Heterogeneities and Rough Interfaces

The importance of small-scale random heterogeneities to seismic wave propagation is well known. There are extensive publications on this subject in seismology. However, the role of random heterogeneities in Lg excitation, propagation, attenuation and blockage, is still unclear due to the complexity of the problem. The theory of wave propagation in unbounded random media has been well developed. However, for waves in complex crustal waveguides with random heterogeneities, the theoretical difficulties are overwhelming, and no analytical tools are available for performing realistic calculations. Numerical simulation is an attractive alternative to theory. Some finite-difference simulations have been conducted (e.g. Frankel and Clayton, 1986; Frankel, 1989; Xie and Lay, 1994; Jih, 1996). Limited by the computation power, however, the finite-difference results are often for short

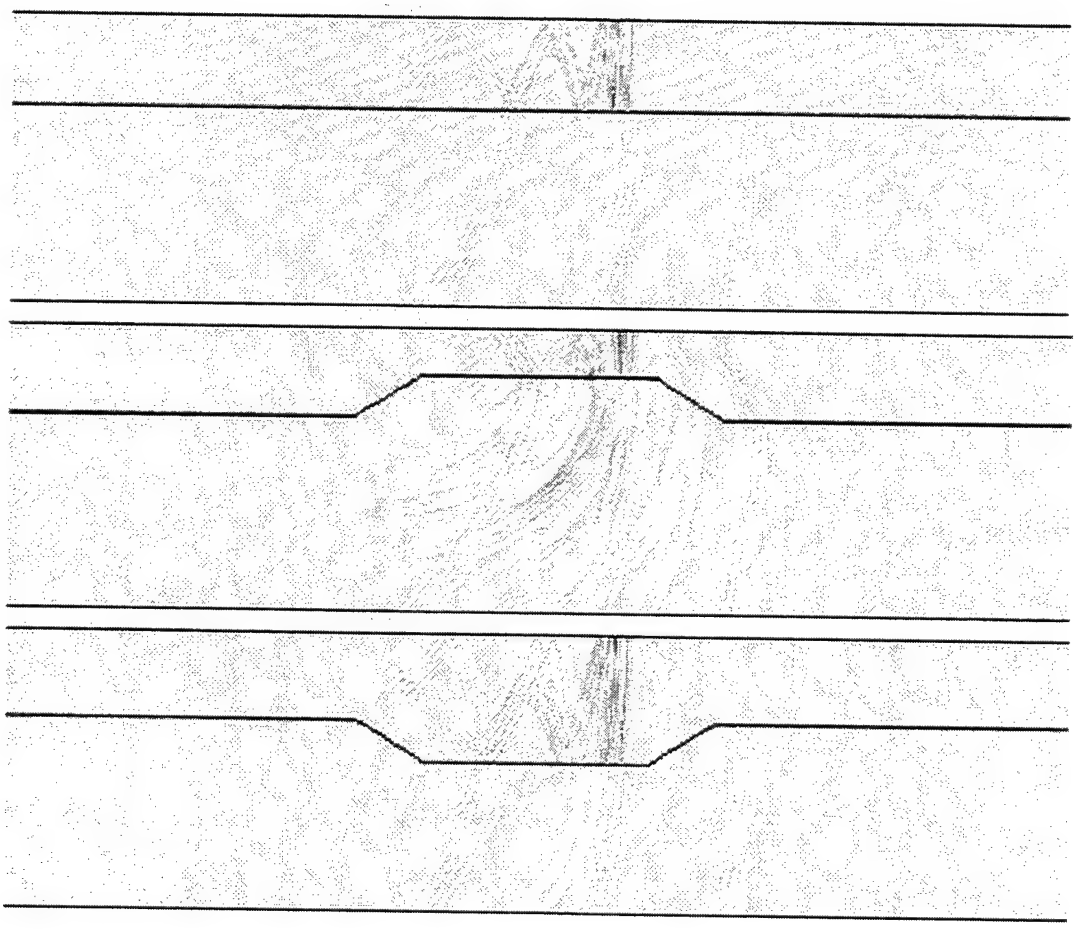

Figure 3: Shown from the top to the bottom are snap-shots at 50 *sec.* for flat, necking and broadening crustal waveguides. The development of mantle wave and head wave, and the formation of multiple reflections between the free surface and the Moho for crustal guided waves can be seen clearly.

Parameters of Crustal Model

Layer	Vs(km/sec)	Density(g/cm)	Thickness(km)
1	3.00	2.60	1.00
2	3.46	2.80	14.00
3	3.76	3.00	22.00
4	4.65	3.30	Half-Space

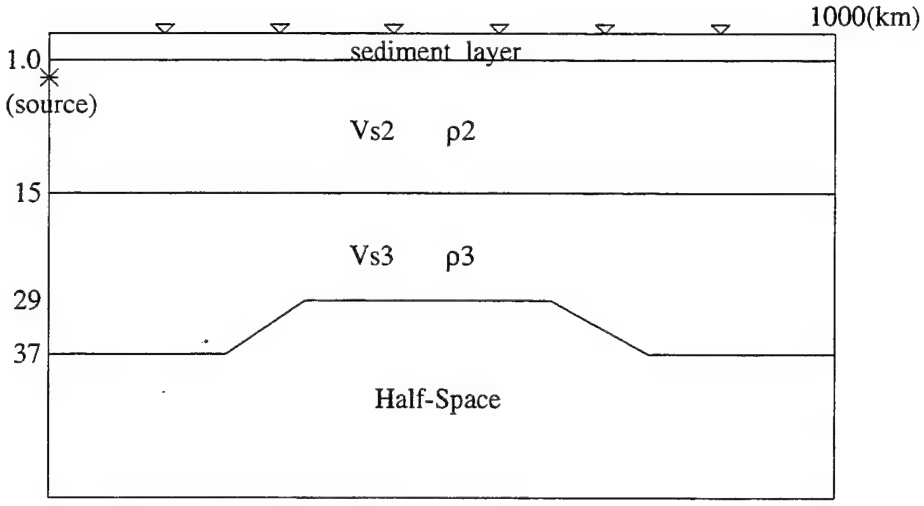

Crustal Model

Figure 4: Flora-Asnes crust model. Shown in the upper panel are model parameters and the lower panel gives the geometry of the model. There is a low velocity sedimentary layer in the top 1 km and a velocity discontinuity at a depth of 15 km. The receivers are on the surface and shown by triangles.

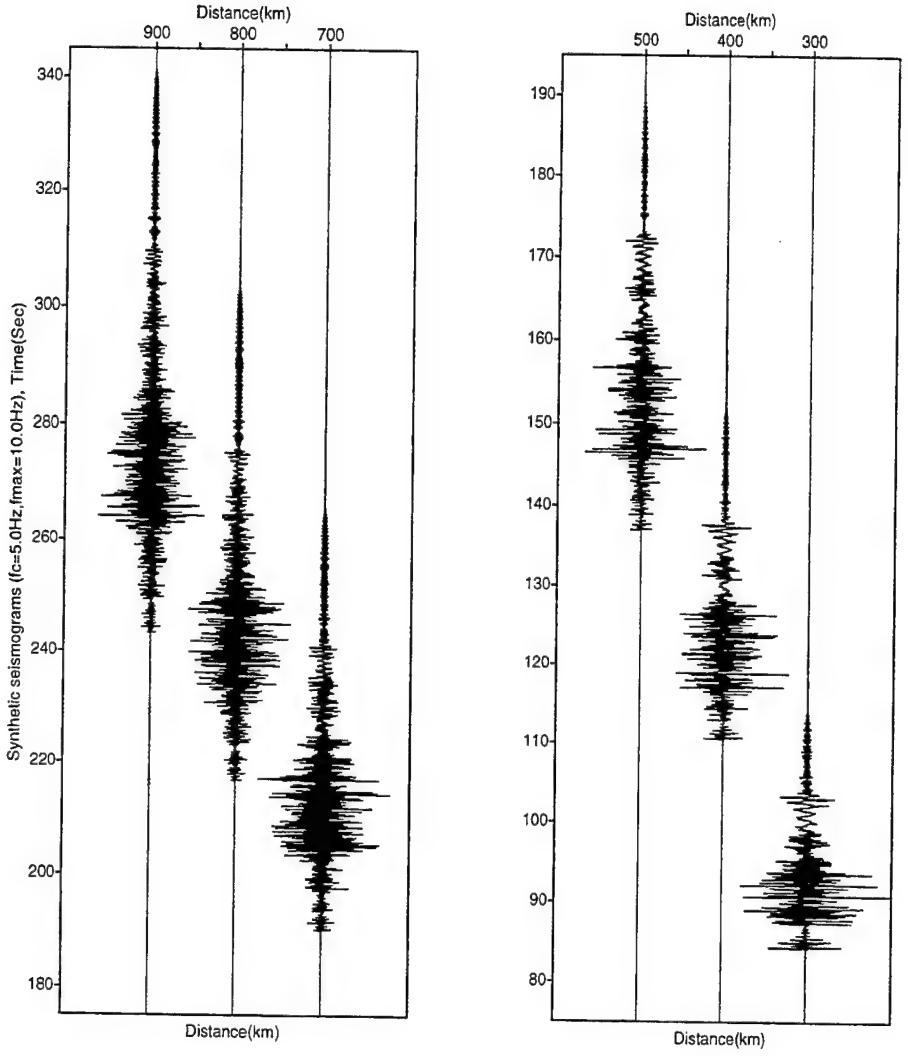

Figure 5: High-frequency synthetic seismograms on the surface at distances up to 1000 km for an inhomogeneous crustal waveguide. The left panel shows synthetics for long distances (up to 1000 km) and the right panel shows synthetics of short distances (up to 350 km).

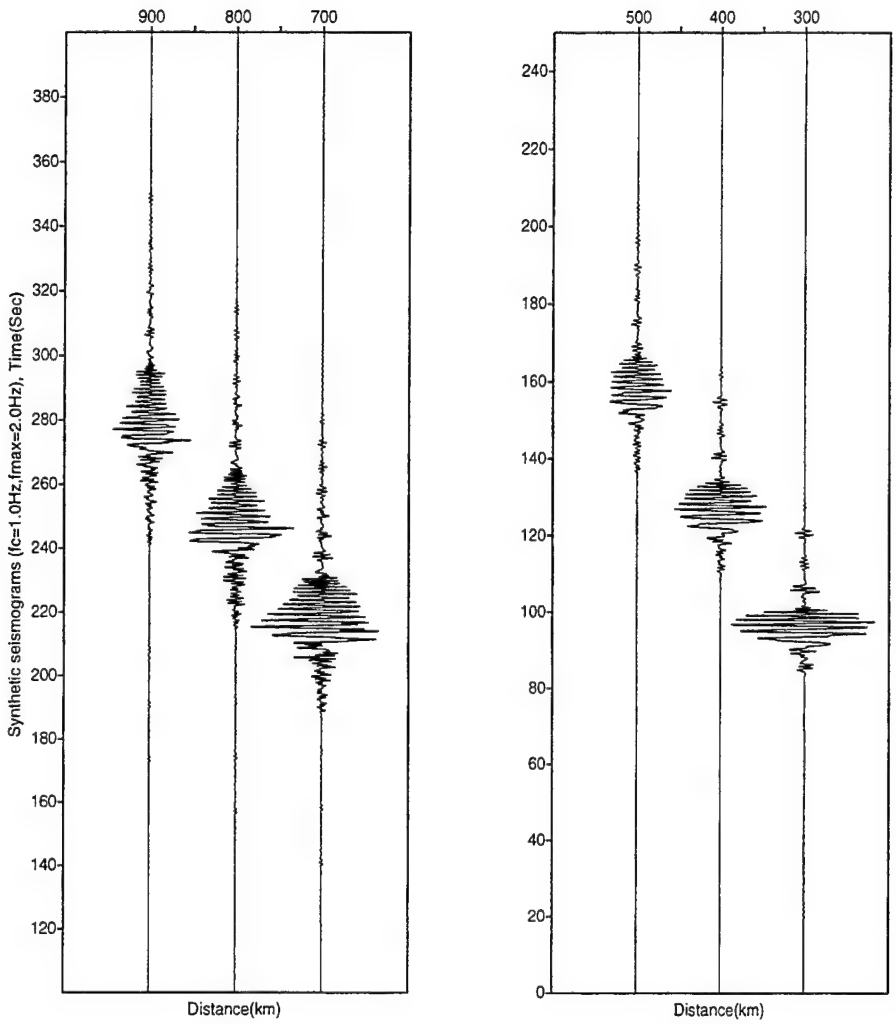

Figure 6: Low-frequency synthetic seismograms on the surface at distances up to 1000 *km* for an inhomogeneous crustal waveguide (Figure 4). The left panel shows synthetics for long distances (up to 1000 km) and the right panel shows synthetics for short distances (up to 350 km).

distances or low frequencies. Liu and Wu (1994) have done some numerical simulation using the phase-screen method, but the media simulated are limited to unbounded media. The development of the half-space GSP method enables us to simulate high-frequency waves propagating in complex crustal waveguides to long distances. In the following, we will show two examples demonstrating the capability of the method.

Figure 7 shows a heterogeneous crustal model representing a 'mountain root' with small-scale random heterogeneities. On the top panel is the velocity model, and the comparisons between synthetic seismograms with and without random heterogeneities are shown on the middle and bottom panels, respectively. The heterogeneities have an exponential correlation function, with the scale length $a_x = a_z$ = 1.6 km (in horizontal and vertical directions, respectively). The RMS velocity perturbation is 5%. The dominant frequency of the source function is 2 Hz. Figures 8 A and B show the comparison between snapshots for waves passing through the 'mountain root' with and without random heterogeneities, respectively. We see that random heterogeneities drastically increase the leakage of waves to the mantle and the complexity of the waveforms. Extensive numerical experiments will be conducted to study the different influences of various kinds of random heterogeneities. It has been shown that the crustal random heterogeneities are highly anisotropic in scale length (Levander and Holliger, 1992; Holliger and Levander, 1992; Wu et al., 1994). The influences of the random heterogeneities with different stochastic characteristics can be explored systematically.

Figure 9 shows the comparison of synthetic seismograms and snapshots for models with and without a rough interface. Shown on the first panel is a crustal model with a 1 km thick low-velocity top layer. The bottom of the low-velocity layer is a rough interface with 0.2 km RMS random depth fluctuations. The randomness has an exponential correlation function and a horizontal scale length of 0.5km. The source is located at 2 km depth and at zero distance. the receiver is located at the surface and at a distance of 500 km. The second and third panels show the comparison of synthetic seismograms; the bottom two panels show the

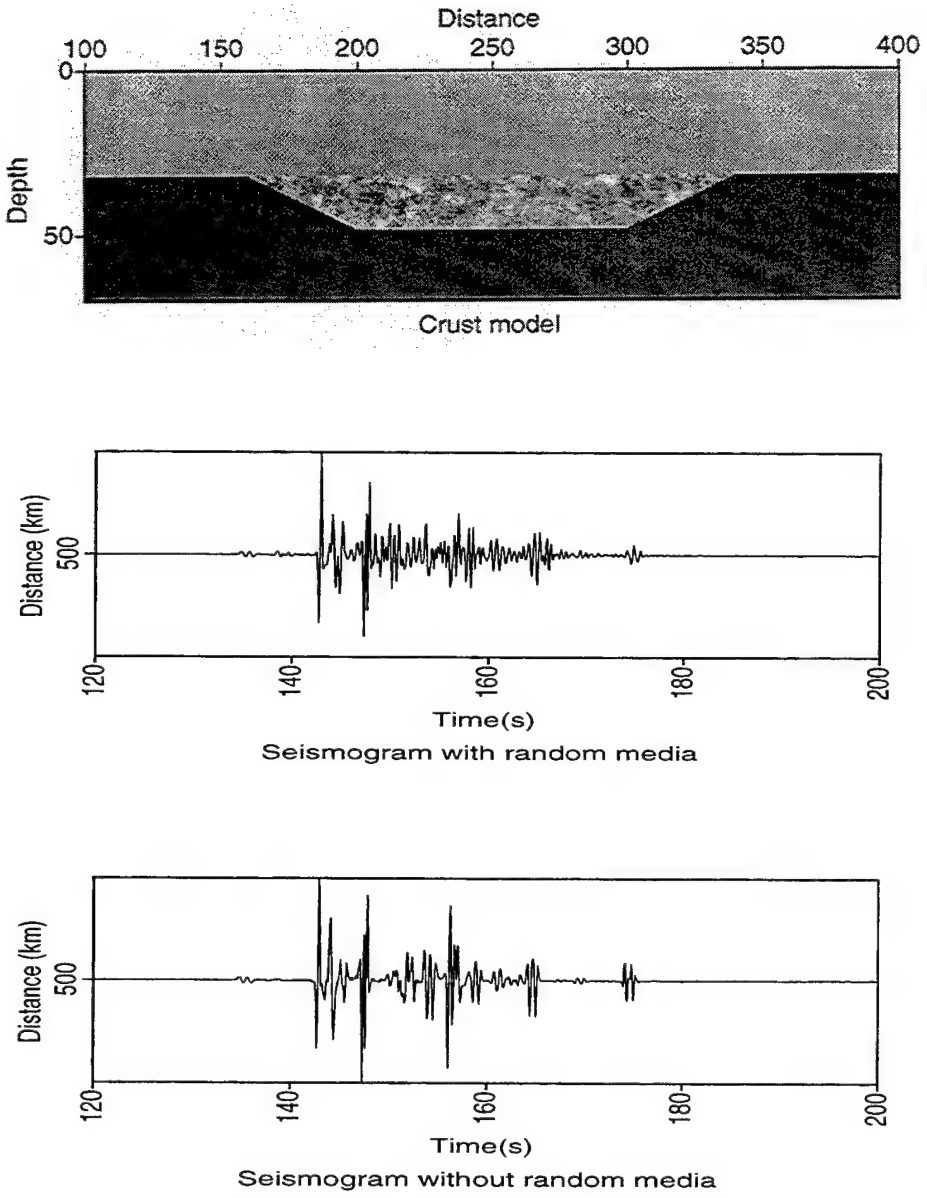

Figure 7: A heterogeneous crustal model representing a mountain root with small-scale random heterogeneities (top panel). Synthetic seismograms with and without random heterogeneities are shown on the middle and bottom panels, respectively. The source is located at a depth of 2 km and zero distance; and the receiver is located on the surface and at a distance of 500 km.

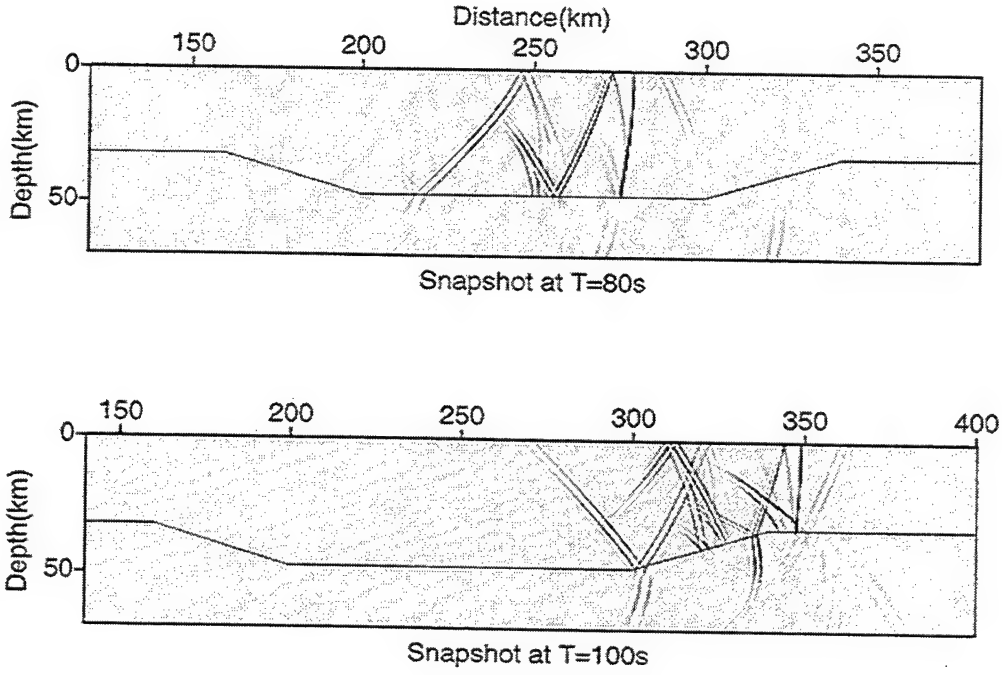

A. Snapshot for waves passing a mountain root without random heterogeneities

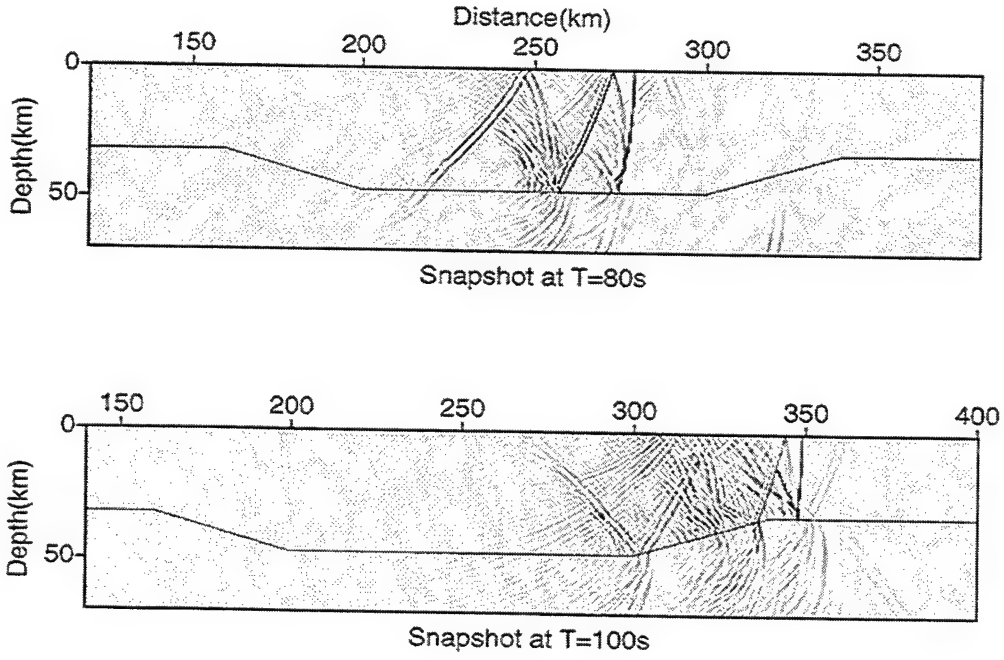

B. Snapshot for waves passing a mountain root with random heterogeneities

Figure 8: Comparison between snapshots for waves passing through a 'mountain root' with or without random heterogeneities, shown on A and B, respectively.

comparison of snapshots. We see that rough interfaces of sedimentary layers can also increase the mantle leakage and waveform complexity of regional waves.

In the following, we will test and discuss how these small scale structures affect Lg energy transport. Before applying the screen propagator method to a random velocity model, we first check the validity of the screen method by comparing its result with that from a finite-difference method. The upper panel of Figure 10 gives a random velocity model with 5% RMS velocity perturbation and a correlation length of 1 km (exponential correlation function) in the crust. To shorten the computation time, we used a 16 km thick crust. The source is located at a depth of 2 km and at the zero distance. A receiver array is put on the free surface from zero distance to 250 km. Both finite-difference method and screen method are used to calculate the synthetic seismograms for the same model. The wave energy are then calculated from these synthetic seismograms. The lower panel shows the comparison of relative energy decay curves between these two methods. The solid line is from the finite-difference method and the dotted line is from the screen propagator method. The agreement between these two methods is quite well. This proves the validity of the screen propagator applied to the energy transfer and partition in random crustal waveguides. For this test model, the FD calculation has $\Delta x = \Delta z = 0.125km$, $\Delta t = 0.015$ sec, resulting in a CPU time of 58 hours on a SUN SPARC-4 work station, while the screen method has $\Delta x = \Delta z = 0.25km$, $\Delta t = 0.1$ sec., and a CPU time of 0.5 hour on the same machine. Both calculations have $f_0 = 1$ Hz. For the screen method, the cutoff frequency $f_{max} = 2$ Hz.

The next test is for a normal crustal waveguide with a 5% RMS random velocity perturbations in the crust. The fluctuation has an exponential power spectrum with different scales. Figure 11 gives the attenuation curves for different characteristic scales. The upper panel is the relative total energy, which is the energy contained in the whole seismogram recorded on the surface versus distance. The solid line is for $ka = 1$, the dotted line is for $ka = 10$, where k is wavenumber and a is the correlation length of the random perturbations; and the dashed line is for the reference model without heterogeneities. We see that for the reference

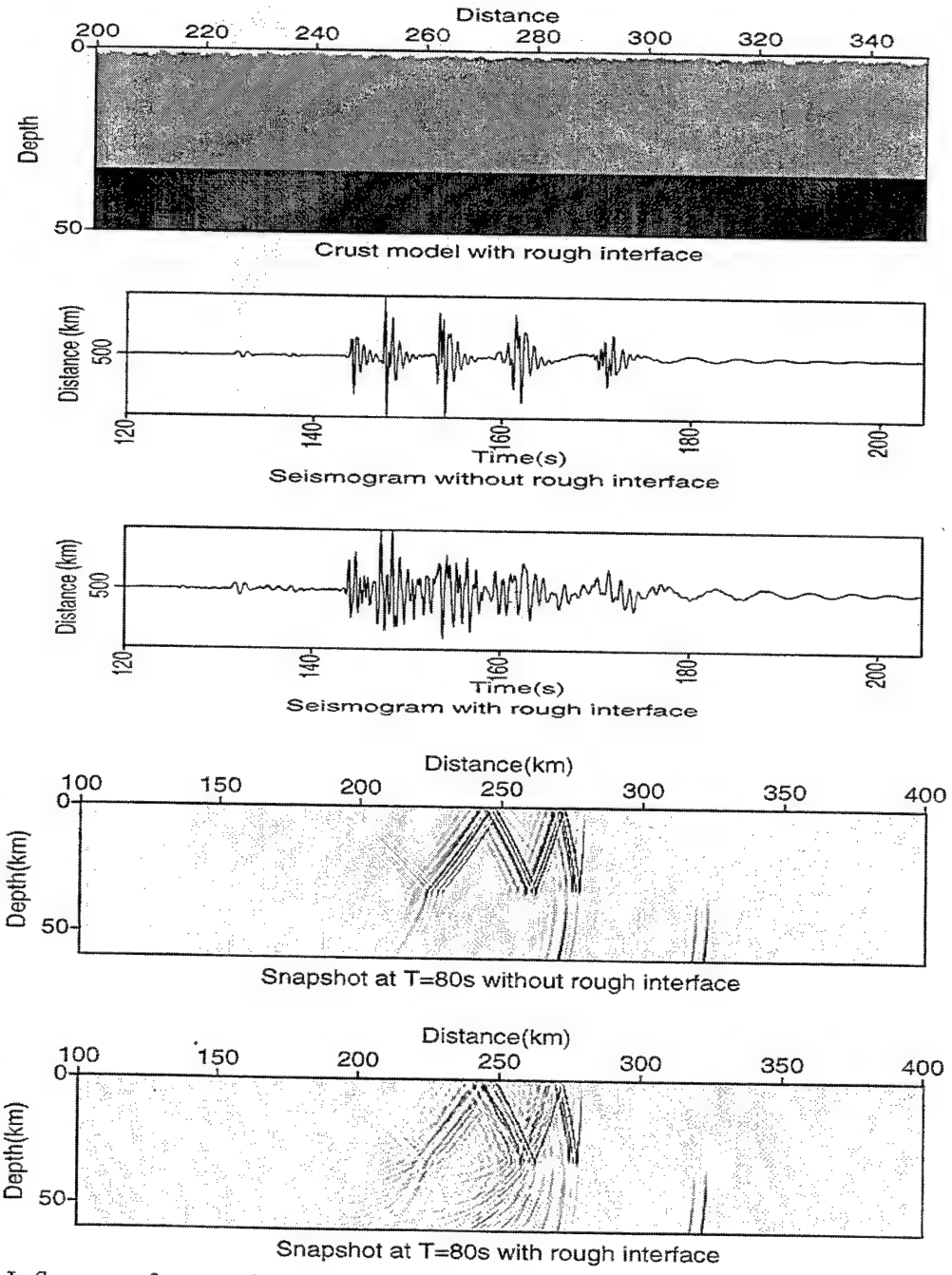

Figure 9: Influence of a rough interface on Lg propagation. The top panel is a crustal model with a sedimentary layer for which the bottom is a rough interface. The source and receiver are located at (0, 2) and (500, 0). The second and third panels show the comparison of synthetic seismograms; the bottom two panels show the comparison of snapshots.

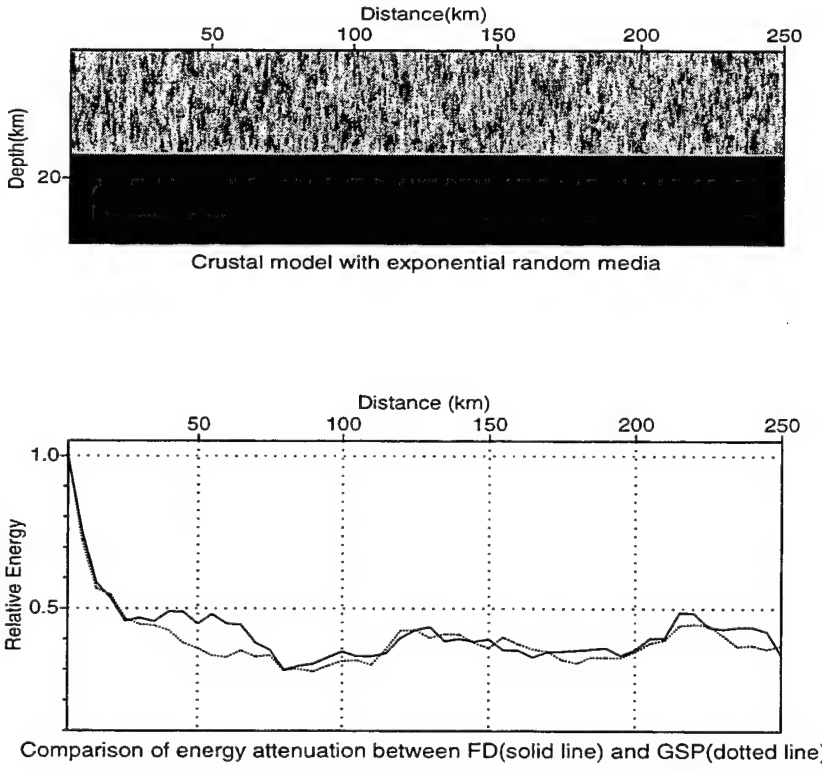

Figure 10: Comparison of energy attenuation curves calculated by screen propagator method and finite-difference method. Shown in the top panel is the velocity structure including random heterogeneities and in the lower panel are the energy attenuation curves.

model, the total energy remains basically constant beyond critical distance, which serves as a checking point for the numerical simulations. The lower panel gives the logarithmic relative RMS Lg wave amplitudes, which are calculated within the Lg window, versus distance. Again, the solid, dashed and dotted lines are for $ka = 1$, $ka = 10$ and the reference model. In both measurements $ka = 1$ lines give stronger attenuation than $ka = 10$ lines. We see also that the Lg amplitudes attenuate more rapidly than the total energy. This is due to the effect of scattering, which diffuses the waves out of the Lg window.

The existence of rough surface and interfaces has effects on both excitation and propagation of Lg-waves. First, the rough surface near the source region may affect the source energy partitioning. Second, along the entire propagation path, the trapped energy in the waveguide may be redirected to steeper angles due to scattering, causing it to leak into the upper mantle. This can cause additional Lg-wave attenuation. Similar to the example shown above, we use a low velocity layer with a rough lower interface to simulate the effect of a rough surface. In Figure 12, the upper panel is the velocity structure including a surface sedimentary layer with a random interface. The sedimentary layer has an average thickness of 1 km and a RMS depth perturbation of 0.2 km with correlation length of 1 km. The middle panel is the energy distribution versus distance and vertical slowness. It clearly shows that with the existence of a rough interface, considerable energy moves from lower vertical slowness to higher vertical slowness. In other words, the energy propagation directions are deflected from near horizontal to steeper directions, which makes more energy leak into the upper mantle and causes extra Lg wave attenuation. The lower panel gives the energy attenuation curves versus distance, in which the solid line is for the model with a rough interface and the dotted line is for the reference model. It shows clearly the effect of a rough interface on Lg attenuation.

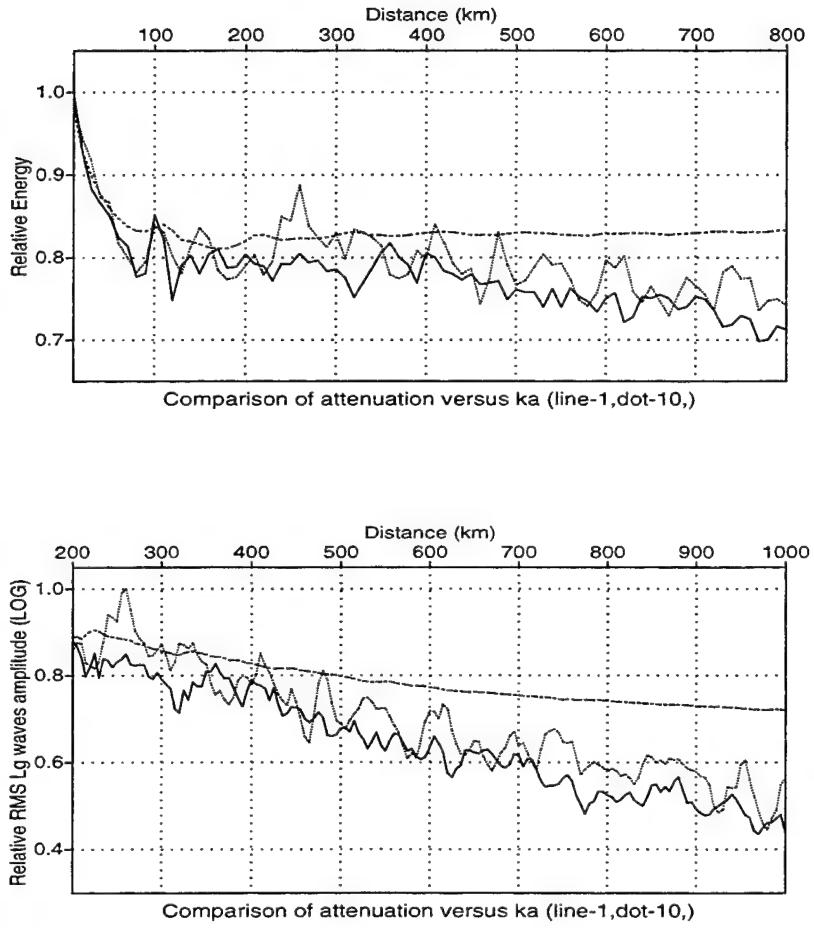

Figure 11: Attenuation curves for a flat crust with random heterogeneities having different characteristic scales. The upper panel is the relative energy attenuation, and the lower panel is the logarithmic relative RMS Lg wave amplitude attenuation. The solid line is for $ka = 1$, the dotted line is for $ka = 10$, where a is the correlation length, and the dashed line is for the reference model.

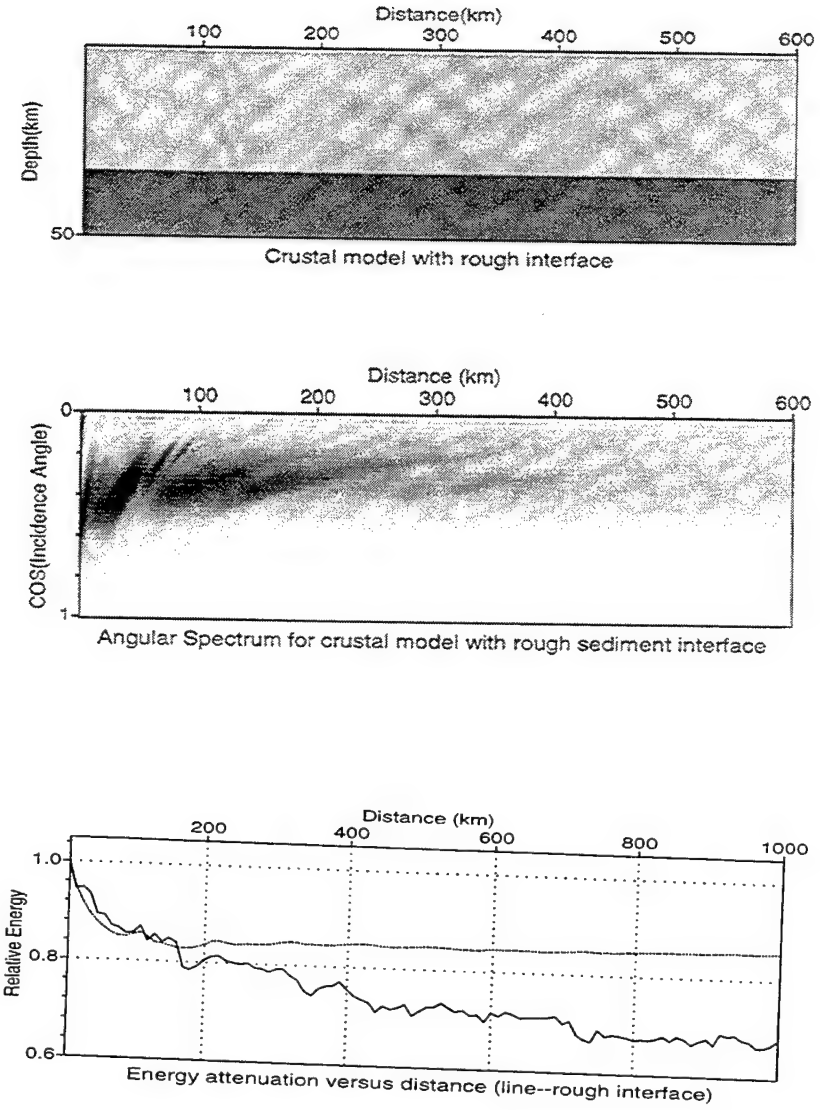

Figure 12: Energy distribution for a crustal waveguide model with rough sedimentary interface. From top to bottom, crustal structure; energy distribution versus vertical slowness and distance; and energy attenuation versus distance. Dotted line indicates propagation through reference model; solid line through model with rough interface.

3 Global Generalized Reflection/Transmission Matrix Method

The discretization of BIE can be done by integration of the Green's function either in space domain (e.g. Sanches-Sesma and Campillo, 1991), or in wavenumber domain using the discrete wave number representation (Bouchon, 1985; Campillo and Bouchon, 1985; Chen, 1990, 1995, 1996). In the latter approach, the singularity problem of the Green's function is avoided by using truncated series. The wavenumber domain BIE has another advantage that it can be easily extended to the case of multilayered media with irregular interfaces. In Bouchon et al. (1989), propagator matrices are used to relate equivalent force distributions on neighboring interfaces. Chen (1990, 1995, 1996) related the fields at neighboring layers by global reflection/transmission coefficients and then derived the global generalized R/T coefficients to relate observations and sources. In these methods, the dimensionality of the linear system to solve are independent of the number of layers involved. The computation time increases only linearly with the number of interfaces. For this reason, we adopt Chen's GGRTM (Global Generalized Reflection/Transmission Matrix) method as the candidate in our hybrid method.

The GGRTM can be viewed as an extension of the reflectivity method for horizontally layered case to an irregularly layered case, and it has been demonstrated to be an accurate and effective method to simulate seismic waves in laterally varying layered media (Chen, 1991, 1995, 1996). For example, for the scattering problem due to a semi-circular canyon (shown in Figure 13), GGRTM can provide very accurate results. Figures 14 and 15 show the comparisons of the results (solid lines) computed by GGRTM with the analytical solutions of Trifunac (1971,1973) (dotted lines) for various normalized frequencies, showing excellent agreement between them. It is known that in this semi-circular canyon model, there are two sharp edges. Many other methods, e.g., Aki-Larner method, T-matrix method and other high-frequency asymptotic methods, fail to provide correct solutions.

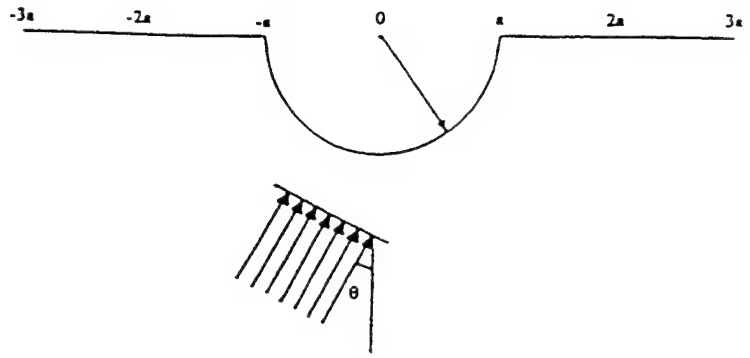

Figure 13: The configuration of the scattering problem due to a semi-circular canyon and an incident plane wave, where a is the radius of the canyon, and θ is the angle of incident wave.

3.1 Connection Formulation

Assume domain II is the model space we are interested in and the field in domain I is easy to calculate by other less expensive methods. According to the representation theorem, wave-fields inside domain II can be expressed as

$$u^{II}(\mathbf{x},\omega) = \int_0^{+\infty} \left\{ \tau^I(\mathbf{x}') + u^I(\mathbf{x}')\mu(z')\frac{\partial}{\partial x'} \right\} G^{II}(\mathbf{x},\mathbf{x}')dz' \tag{17}$$

Where u^I and τ^I are the displacement and traction fields on the vertical boundary surface dividing domain I and II, and can be calculated using methods valid in domain I, μ is the shear rigidity, and G^{II} is the Green's function in domain II which will be calculated by GGRTM.

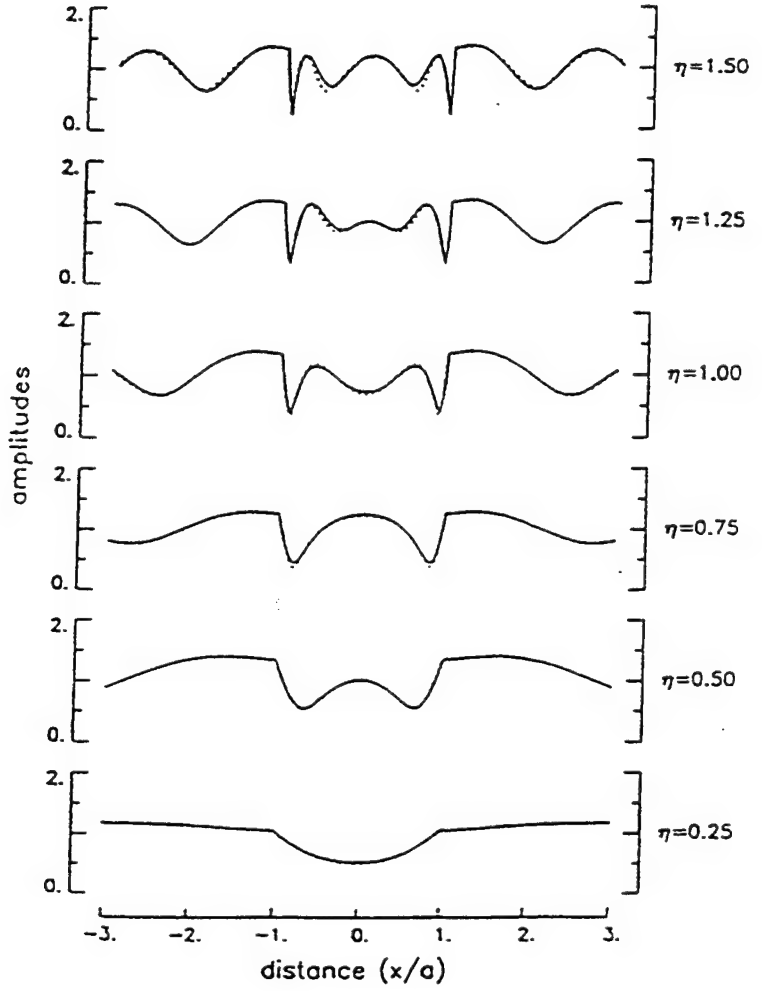

Figure 14: The frequency responses of a semi-circular canyon to vertical incident SH-wave for various normalized frequencies. The solid lines denote our results and the dotted lines denote the exact solutions.

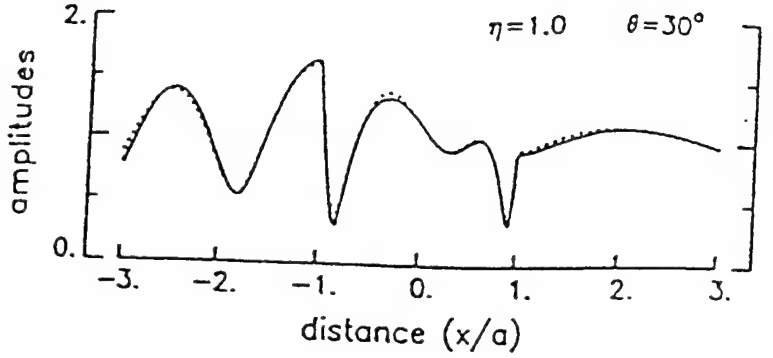

Figure 15: The same response as Figure 14, except that the incident angle is 30°.

3.2 Algorithm of Computing Synthetic Lg Waves

Having the connection formulation, we can use GGRTM to compute synthetic Lg waves. The step-by-step procedure of applying GGRTM to computing a synthetic seismogram in a general irregularly layered medium can be summarized as follows.

Step 1

Calculate the interface matrices for each interface, $\mathbf{Q}_{\downarrow\uparrow}^{(j)}$, $\mathbf{Q}_{\uparrow\downarrow}^{(j)}$, $\mathbf{Q}_{\uparrow\uparrow}^{(j)}$, $\mathbf{Q}_{\downarrow\downarrow}^{(j)}$, $\mathbf{P}_{\uparrow\uparrow}^{(j)}$, $\mathbf{P}_{\downarrow\downarrow}^{(j)}$, $\mathbf{P}_{\uparrow\downarrow}^{(j)}$, $\mathbf{P}_{\downarrow\uparrow}^{(j)}$; for j=1,2, ..., N, by carrying out the integrals over each interface. These interface matrices contain the structural information of the media and are defined as (Chen, 1990)

$$\left(\mathbf{Q}_{\downarrow\uparrow}^{(j)}\right)_n = \frac{-1}{2\nu_n^{(j)} L} \int_{-L/2}^{L/2} \left\{\dot{\xi}^{(j-1)}(x) k_n + \nu_n^{(j)}\right\} \exp[i\Xi_{\downarrow\uparrow}^{(j)}(x,n,m)] dx \ , \qquad (18)$$

$$\left(\mathbf{Q}_{\downarrow\downarrow}^{(j)}\right)_n = \frac{-1}{2\nu_n^{(j)} L} \int_{-L/2}^{L/2} \left\{\dot{\xi}^{(j-1)}(x) k_n - \nu_n^{(j)}\right\} \exp[i\Xi_{\downarrow\downarrow}^{(j)}(x,n,m)] dx \ , \qquad (19)$$

$$\left(\mathbf{Q}_{\uparrow\downarrow}^{(j)}\right)_n = \frac{-1}{2\nu_n^{(j)}L}\int_{-L/2}^{L/2}\left\{\dot{\xi}^{(j)}(x)k_n - \nu_n^{(j)}\right\}\exp[i\Xi_{\uparrow\downarrow}^{(j)}(x,n,m)]dx\,, \tag{20}$$

$$\left(\mathbf{Q}_{\uparrow\uparrow}^{(j)}\right)_n = \frac{-1}{2\nu_n^{(j)}L}\int_{-L/2}^{L/2}\left\{\dot{\xi}^{(j)}(x)k_n + \nu_n^{(j)}\right\}\exp[i\Xi_{\uparrow\uparrow}^{(j)}(x,n,m)]dx\,, \tag{21}$$

$$\left(\mathbf{P}_{\downarrow\uparrow}^{(j)}\right)_n = \frac{-\nu_m^{(j)}}{2\nu_n^{(j)}L}\int_{-L/2}^{L/2}\left\{1+[\dot{\xi}^{(j-1)}(x)]^2\right\}^{12}\exp[i\Xi_{\downarrow\uparrow}^{(j)}(x,n,m)]dx\,, \tag{22}$$

$$\left(\mathbf{P}_{\downarrow\downarrow}^{(j)}\right)_n = \frac{-\nu_m^{(j)}}{2\nu_n^{(j)}L}\int_{-L/2}^{L/2}\left\{1+[\dot{\xi}^{(j-1)}(x)]^2\right\}^{12}\exp[i\Xi_{\downarrow\downarrow}^{(j)}(x,n,m)]dx\,, \tag{23}$$

$$\left(\mathbf{P}_{\uparrow\downarrow}^{(j)}\right)_n = \frac{-\mu^{(j+1)}\nu_m^{(j+1)}}{2\mu^{(j)}\nu_n^{(j)}L}\int_{-L/2}^{L/2}\left\{1+[\dot{\xi}^{(j)}(x)]^2\right\}^{12}\exp[i\Xi_{\uparrow\downarrow}^{(j)}(x,n,m)]dx\,, \tag{24}$$

and

$$\left(\mathbf{P}_{\uparrow\uparrow}^{(j)}\right)_n = \frac{-\mu^{(j+1)}\nu_m^{(j+1)}}{2\mu^{(j)}\nu_n^{(j)}L}\int_{-L/2}^{L/2}\left\{1+[\dot{\xi}^{(j)}(x)]^2\right\}^{12}\exp[i\Xi_{\uparrow\uparrow}^{(j)}(x,n,m)]dx\,, \tag{25}$$

where $\xi^{(j)}(x)$ is the height of the topography for the jth interface, and

$k_n = 2\pi nL$ $\nu_n^{(j)} = \sqrt{(\omega\beta^{(j)})^2 - (k_n)^2}$, and $\mathrm{Im}\left\{\nu_n^{(j)}\right\} \geq 0$,

$$\Xi_{\uparrow\uparrow}^{(j)}(x,n,m) = (k_m - k_n)x + \nu_n^{(j)}[\xi^{(j)}(x) - \xi_{\min}^{(j)}] + \nu_m^{(j+1)}\left|\Delta\xi^{(j)}(x)\right|\,,$$

$$\Xi_{\downarrow\uparrow}^{(j)}(x,n,m) = (k_m - k_n)x + \nu_n^{(j)}[\xi^{(j-1)}(x) - \xi_{\min}^{(j-1)}] + \nu_m^{(j)}\left|\Delta\xi^{(j-1)}(x)\right|\,,$$

and

$$\Xi_{\downarrow\downarrow}^{(j)}(x,n,m) = (k_m - k_n)x - \nu_n^{(j)}[\xi^{(j-1)}(x) - \xi_{\max}^{(j-1)}] + \nu_m^{(j)}\left|\Delta\xi^{(j-1)}(x)\right|\,;$$

for j = 1, 2, ..., N.

Where $\Delta\xi^{(j)}(x) = \xi^{(j)}(x) - z^{(j)}$.

Step 2

Calculate the global modified reflection and/or transmission matrices, { $\mathbf{R}_{\downarrow\uparrow}^{(j)}$ $\mathbf{T}_{\uparrow\uparrow}^{(j)}$ $\mathbf{T}_{\downarrow\downarrow}^{(j)}$ $\mathbf{R}_{\uparrow\downarrow}^{(j)}$ }, from the interface matrices using the following formulas:

$$\begin{bmatrix} \mathbf{R}_{\downarrow\uparrow}^{(j)} & \mathbf{T}_{\uparrow\uparrow}^{(j)} \\ \mathbf{T}_{\downarrow\downarrow}^{(j)} & \mathbf{R}_{\uparrow\downarrow}^{(j)} \end{bmatrix} = \begin{bmatrix} \mathbf{Q}_{\uparrow\uparrow}^{(j)} & \mathbf{P}_{\uparrow\uparrow}^{(j)} \\ -\mathbf{Q}_{\downarrow\downarrow}^{(j+1)} & -\mathbf{P}_{\downarrow\downarrow}^{(j+1)} \end{bmatrix} \begin{bmatrix} -\mathbf{Q}_{\uparrow\downarrow}^{(j)} & -\mathbf{P}_{\uparrow\downarrow}^{(j)} \\ \mathbf{Q}_{\downarrow\uparrow}^{(j+1)} & \mathbf{P}_{\downarrow\uparrow}^{(j+1)} \end{bmatrix}^{-1} \begin{bmatrix} \mathbf{E}_{\max}^{(j)} & \\ & \mathbf{E}_{\min}^{(j+1)} \end{bmatrix}, \tag{26}$$

and

$$\mathbf{R}_{\uparrow\downarrow}^{(o)} = -\mathbf{Q}_{\downarrow\downarrow}^{(1)} \left(\mathbf{Q}_{\downarrow\uparrow}^{(1)}\right)^{-1} \mathbf{E}_{\min}^{(1)}, \tag{27}$$

Where $\mathbf{E}_{\min}^{(j)}$ and $\mathbf{E}_{\max}^{(j)}$ are diagonal matrices given by

$$\mathbf{E}_{\min}^{(j)} = diagonal \left\{ \exp[iv_n^{(j)}(\xi_{\min}^{(j)} - \xi_{\min}^{(j-1)})];\ n = 0, \pm 1, \pm 2, ... \right\},$$

and

$$\mathbf{E}_{\max}^{(j)} = diagonal \left\{ \exp[iv_n^{(j)}(\xi_{\max}^{(j)} - \xi_{\max}^{(j-1)})];\ n = 0, \pm 1, \pm 2, ... \right\}.$$

These global modified reflection and/or transmission matrices describe the reflection and/or transmission effects due to a single interface regardless of the influences from other existing interfaces.

Step 3

Compute the global generalized reflection and/or transmission matrices, $\hat{\mathbf{T}}_{\uparrow\uparrow}^{(j)}$, $\hat{\mathbf{R}}_{\downarrow\uparrow}^{(j)}$, $\hat{\mathbf{T}}_{\downarrow\downarrow}^{(j)}$, and $\hat{\mathbf{R}}_{\uparrow\downarrow}^{(j)}$, from the global modified reflection and/or transmission matrices through following recursive formulas:

$$\begin{aligned} \hat{\mathbf{R}}_{\uparrow\downarrow}^{(o)} &= \mathbf{R}_{\uparrow\downarrow}^{(o)} \\ \hat{\mathbf{T}}_{\uparrow\uparrow}^{(j)} &= [\mathbf{I} - \hat{\mathbf{R}}_{\downarrow\uparrow}^{(j)} \hat{\mathbf{R}}_{\uparrow\downarrow}^{(j-1)}]^{-1} \mathbf{T}_{\uparrow\uparrow}^{(j)}, \quad for\ j = 1, 2, ..., N; \\ \hat{\mathbf{R}}_{\downarrow\uparrow}^{(j)} &= \mathbf{R}_{\downarrow\uparrow}^{(j)} + \mathbf{T}_{\downarrow\downarrow}^{(j)} \hat{\mathbf{R}}_{\uparrow\downarrow}^{(j-1)} \hat{\mathbf{T}}_{\uparrow\uparrow}^{(j)} \end{aligned} \tag{28}$$

and

$$\begin{aligned}
\hat{\mathbf{R}}_{\downarrow\uparrow}^{(N+1)} &= 0 \\
\hat{\mathbf{T}}_{\downarrow\downarrow}^{(j)} &= [\mathbf{I} - \hat{\mathbf{R}}_{\uparrow\downarrow}^{(j)}\hat{\mathbf{R}}_{\downarrow\uparrow}^{(j+1)}]^{-1}\mathbf{T}_{\downarrow\downarrow}^{(j)}\ , \quad for\ j = N, N-1, ..., 2, 1. \qquad (29) \\
\hat{\mathbf{R}}_{\uparrow\downarrow}^{(j)} &= \mathbf{R}_{\uparrow\downarrow}^{(j)} + \mathbf{T}_{\uparrow\uparrow}^{(j)}\hat{\mathbf{R}}_{\downarrow\uparrow}^{(j+1)}\hat{\mathbf{T}}_{\downarrow\downarrow}^{(j)}
\end{aligned}$$

These global generalized reflection and/or transmission matrices represent the total reflection and/or transmissions due to the multi-irregular layers.

Step 4

Compute the expansion coefficients of displacement spectra at the free surface,

$$z = \xi^{(0)}(x),$$

by using the formula

$$\underline{\alpha}^{(o)} = \left(\mathbf{Q}_{\downarrow\uparrow}^{(1)}\right)^{-1}\mathbf{E}_{\min}^{(1)}\left\{\hat{\mathbf{s}}_{\uparrow}^{(1)} + \hat{\mathbf{T}}_{\uparrow\uparrow}^{(1)}\hat{\mathbf{s}}_{\uparrow}^{(2)} + \hat{\mathbf{T}}_{\uparrow\uparrow}^{(1)}\hat{\mathbf{T}}_{\uparrow\uparrow}^{(2)}\hat{\mathbf{s}}_{\uparrow}^{(3)} + ... + \hat{\mathbf{T}}_{\uparrow\uparrow}^{(1)}\hat{\mathbf{T}}_{\uparrow\uparrow}^{(2)}...\hat{\mathbf{T}}_{\uparrow\uparrow}^{(N)}\hat{\mathbf{s}}_{\uparrow}^{(N+1)}\right\}\ , \qquad (30)$$

where $\hat{\mathbf{s}}_{\uparrow}^{(j)}$ is the equivalent source term for the jth layer derived by the representation theorem and

$$\hat{\mathbf{s}}_{\uparrow}^{(j)} = \left\{\mathbf{I} - \hat{\mathbf{R}}_{\uparrow\downarrow}^{(j-1)}\hat{\mathbf{R}}_{\downarrow\uparrow}^{(j)}\right\}^{-1}\left(\mathbf{s}_{\uparrow}^{(j)} + \hat{\mathbf{R}}_{\downarrow\uparrow}^{(j)}\mathbf{s}_{\downarrow}^{(j)}\right)\ , \qquad (31)$$

$$\left(\mathbf{s}_{\uparrow}^{(j)}\right)_n = \frac{i}{2\nu_n^{(s)}L}\int_{-L/2}^{L/2} dx \int_{\xi^{(j-1)}(x)}^{\xi^{(j)}(x)} f^{(j)}(x,z)\exp[-ik_n x + i\nu_n^{(j)}(z - \xi_{\min}^{(j)})]dz\ , \qquad (32)$$

$$\left(\mathbf{s}_{\downarrow}^{(j)}\right)_n = \frac{i}{2\nu_n^{(j)}L}\int_{-L/2}^{L/2} dx \int_{\xi^{(j-1)}(x)}^{\xi^{(j)}(x)} f^{(j)}(x,z)\exp[-ik_n x - i\nu_n^{(j)}(z - \xi_{\max}^{(j-1)})]dz\ , \qquad (33)$$

for j =1, 2, ..., N, N+1;

and

$$f^{(j)}(x,z) = \left\{\tau^{(j)}(x,z) + \mu^{(j)}u^{(j)}(x,z)\frac{\partial}{\partial x}\right\}\ . \qquad (34)$$

Step 5

Calculate the displacement spectra at the free surface by using the following formula:

$$W^{(o)}[x, \xi^{(o)}(x), \omega] = \sum_{m=-M}^{M} \alpha_m^{(o)} \exp\left\{ik_m + i\nu_m^{(1)} \left|\Delta\xi^{(o)}(x)\right|\right\} . \qquad (35)$$

Taking the Fourier transform of the above frequency domain solution, we can finally obtain the time domain solution, i.e., the synthetic seismogram.

3.3 Numerical Test

To test the validity of our hybrid method, we consider a trivial case: a laterally homogeneous layered case. This problem can be fully solved by the reflectivity method. To test our algorithm, we use our hybrid method to synthesize the seismograms, then check the results with the reflectivity method. The test model is a single layer crustal model. The velocities and densities of the crust and mantle are 3.5 km/sec, 2.8 g/cm^3, 4.5 km/sec and 3.2 g/cm^3, respectively. The thickness of the crust is 32 km, the seismic source is buried at z_s=2 km and x_s=0 km. Receiver is placed at z_0=0 km and x_0=250 km. The connection boundary is located at x=150 km. The synthetic seismogram of the reflectivity method is plotted in Figure 16a. The synthetic seismogram of GGRTM is shown in Figure 16b, Comparison of these two seismograms shows excellent agreement between the hybrid method and the reflectivity method, confirming the validity of the connection scheme for our hybrid method.

The computer code for calculating general irregular media is under development at this stage, and is expected to be finished soon. We will then calculate synthetic Lg waves propagating through an arbitrarily irregular layered medium to study the influence of surface topography and interface irregularities.

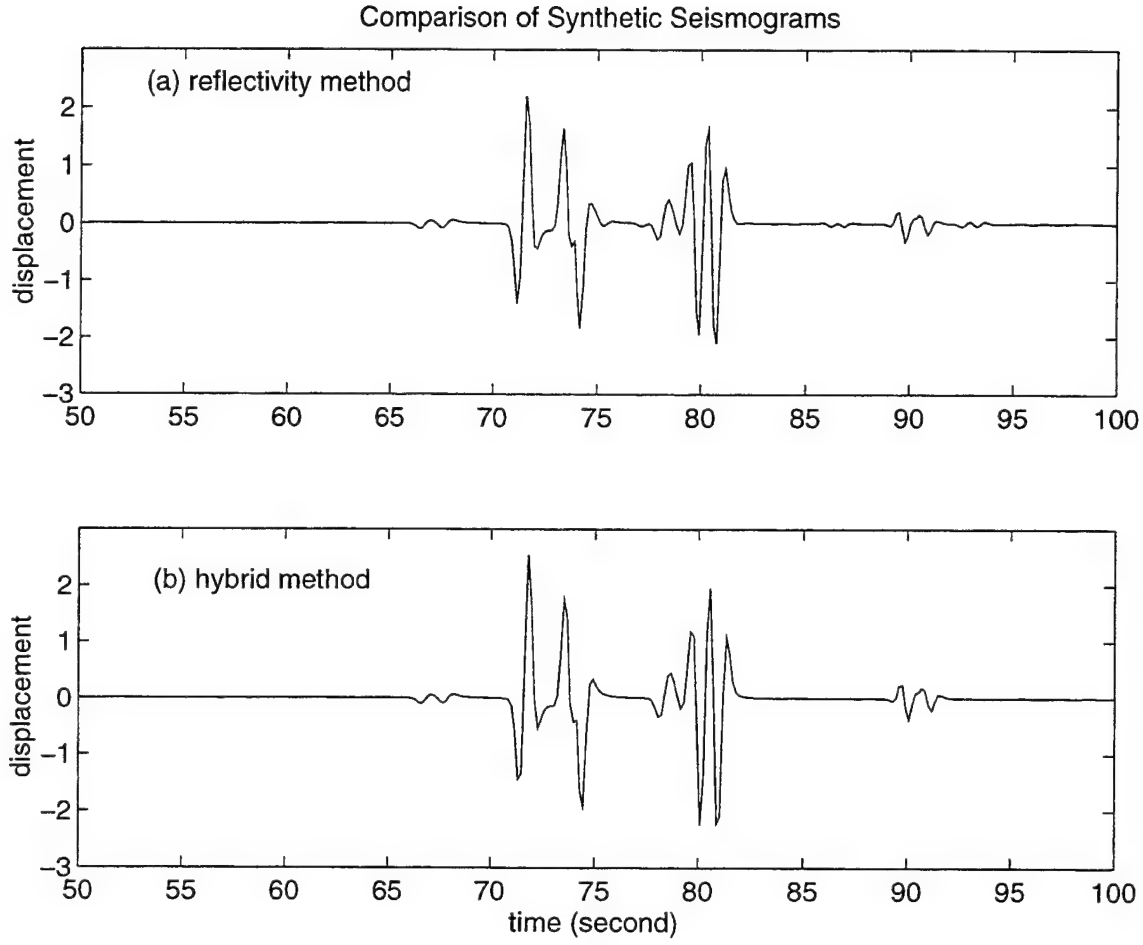

Figure 16: Comparison of synthetic seismograms for a laterally homogeneous layered crustal model. A: synthetic seismogram from reflectivity method, and B: synthetic seismogram from hybrid method.

4 A Generalized Screen - Boundary Element Hybrid Method

4.1 Boundary Element Methods

In many cases, wave propagation involving heterogeneous media can be formulated in terms of boundary integral equations. The strict boundary methods include the direct and indirect boundary integral equation techniques. The direct method has been widely used due to the explicit meaning of the unknowns in the formulation, while the indirect method formulates problems in terms of force or force moment boundary densities. These two methods can be implemented either in the space-time domain or in the space-frequency domain.

For many applications, an alternative approach has been developed by the combination of discrete wavenumber expansions for Green's functions with boundary integral formulations (Bouchon, 1985; Campillo and Bouchon, 1985; Bouchon et al., 1989). In this case, the singularity problem of the Green's function is avoided by using wavenumber integration. This technique has been shown to be accurate for any finite frequency and can be extended for multilayered media with irregular interfaces. This method is still limited to the case of low frequencies due to the computational intensity.

In this study, we select the direct frequency-domain BE method integrated with the screen approach to model the effects of both local irregular topography and complex crustal structure on regional wave propagation. In application to the problem of regional wave propagation, Gibson and Campillo (1994) have used the BE method for frequencies up to 1 Hz. The computation at higher frequencies becomes extremely time consuming because matrices with large size must be inverted. In fact, the propagation properties deduced from simulations at relatively low frequencies on the order of 1 Hz show very different characteristics from those with higher frequencies (Wu et al., 1996). By using the hybrid scheme, the relatively short sections of the local strong heterogeneities including irregular topography in

the crustal waveguide can be modeled by the BE method to high frequencies, and the exterior field in the relative weak heterogeneous media of large volume can be calculated by the screen method.

The formulation of the BE method can be briefly described as follows. Consider steady state scalar wave propagation in a homogeneous region Ω bounded by a boundary Γ . Assuming a point source is located at $\mathbf{r}_0$, with a source function $S(\omega)$, the boundary integral equation for the seismic response $u(\mathbf{r})$ at location $\mathbf{r}$ on Γ can be written as

$$C(\mathbf{r})u(\mathbf{r}) + \int_\Gamma u(\mathbf{r}')\frac{\partial}{\partial n}G(\mathbf{r},\mathbf{r}')d\mathbf{r} = \int_\Gamma G(\mathbf{r},\mathbf{r}')\frac{\partial}{\partial n}u(\mathbf{r}')d\mathbf{r}' + S(\omega)G(\mathbf{r},\mathbf{r}_0), \quad (36)$$

where the coefficients $C(\mathbf{r})$ generally depends on the local geometry at $\mathbf{r}$, $G(\mathbf{r},\mathbf{r}')$ is the Green's function for the homogeneous region, $\partial/\partial n$ denotes differentiation with respect to the outward normal of the boundary Γ, and $S(\omega)$ is the source spectrum.

In this study we adopt the strict frequency-space domain BE method. The boundary Γ is discretized into a finite number of elements. The boundary integral eq. (1) for all nodes is approximated by a simultaneous system of linear equations. In general, the coefficient matrix is full-rank. For a piecewise homogeneous media with irregular interfaces (Fu and Mu, 1994; Fu, 1996), the discretization of eq. (1) can be done in each subdomain, and then all equations are assembled into a global matrix equation by using the interface conditions of continuity for displacements and their normal gradients across all interfaces. This global matrix is sparse or narrow-banded, depending on the structure of the models. Since matrix operations are involved and the matrix for each frequency component must be inverted, the BE method is not efficient for the large volume problem. This problem can be circumvented with the use of hybrid methods.

Figure 17 shows the application of the BE method to a 2-D complex salt model in Figure 17a. The medium is piecewise homogeneous, with the wave velocities indicated in the figure. The dimensions of the model are 4000 m horizontally and 900 m vertically. The source is a minimum-phase wavelet with a central frequency of

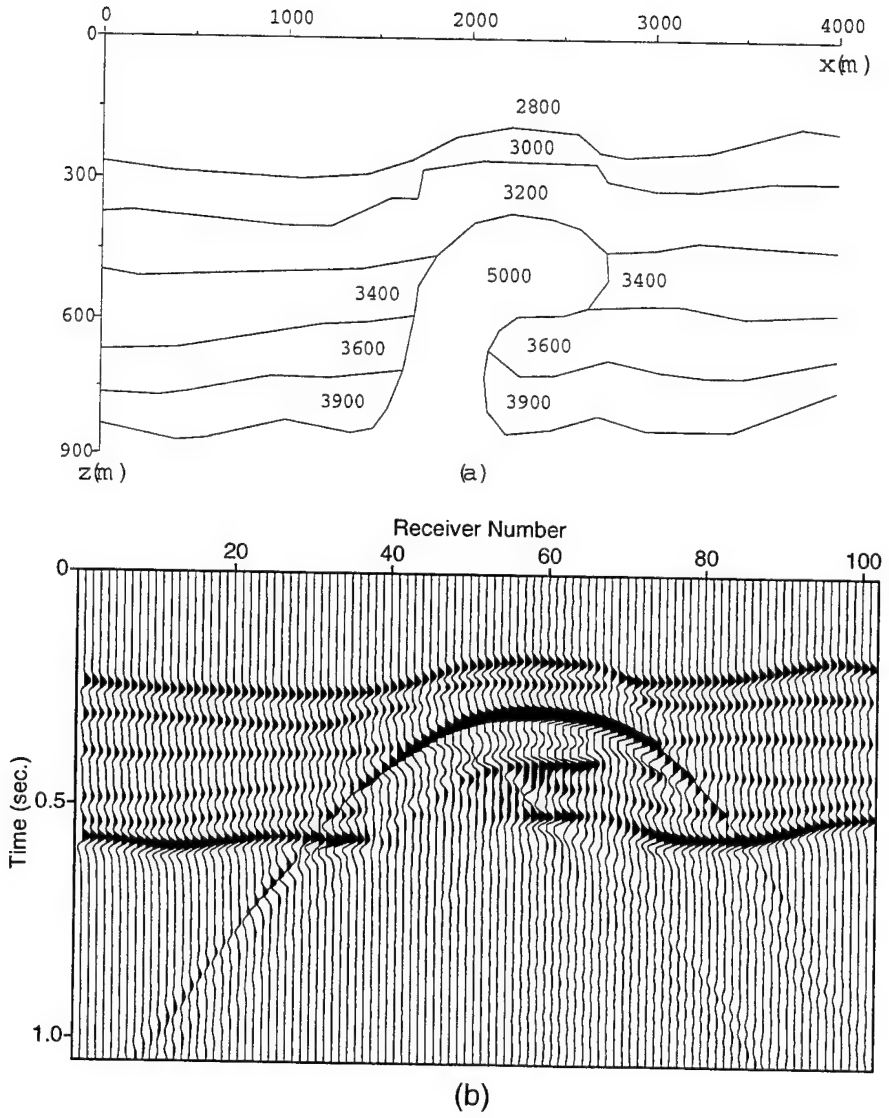

Figure 17: (a) The geometry of a 2-D salt model. The velocity unit is m/s. (b) The Synthetic acoustic seismograms calculated with the BE method.

20 Hz. The synthetic seismograms for coincident source-receiver configurations are displayed in Figure 17b with receivers 1 to 101 located at 0 to 4000 m along the x-axis. Wave fields are calculated in the frequency range 0 - 40 Hz on a PC computer with Intel 166 MHz Pentium Processor. A variable element dimension technique in the program implementation is adopted to improve the computation speed. The element dimension for each frequency is computed according to the medium velocity and the frequency, and then the model is automatically discretized. This improves the efficiency of the BE method.

4.2 A GS-BE Hybrid Scheme

Although the use of the boundary method lags far behind the use of domain methods (e.g., finite-difference or finite-element methods) in engineering, it has been extensively used to study the effects of topography or sedimentary basin structures on ground motions at the surface during the last two decades (Lee and Langston, 1983; Gaffet and Bouchon, 1989; Sanchez-Sesma et al., 1989; Sanchez-Sesma and Campillo, 1991; 1993; Benites and Aki, 1989; Papageorgiou and Kim, 1993; Kim and Papageorgiou, 1993; and has gained popularity among theoretical seismologists. This approach has also been used to study the Lg blockage problem with limited success. Blockage is assumed to be caused by coastlines, mountains and sudden change of crustal thickness. However, numerical simulations of blockage by large-scale crustal structures by using finite difference and boundary methods have not succeeded in matching the observations (Campillo, 1993; Gibson and Campillo, 1994). Geological structures such as grabens and mountain ranges often lead to anomalous attenuation, even extinction of the Lg phases. However, based on the synthetic seismograms using these methods, the Lg waves should propagate with a much smaller degree of amplitude reduction than is observed. One of the reasons for these discrepancies between the observed and modeling results is that the models used were oversimplified and did not include small-scale irregularities.

The hybrid method will combine the screen method and the BE method so

that the expensive BE calculations can be limited to relatively short sections with severe surface topography. The boundary connection technique to couple the fields calculated by the screen method with those of the BE method will play a crucial role in the hybrid method. The BE method is a well-tested numerical method. For the accuracy of the screen method, extensive numerical tests have been done (Liu and Wu, 1994; Wu et al., 1996; Huang and Fehler, 1998) in comparison with various other numerical methods. The accuracy of the hybrid scheme depends on these two methods and their connection.

4.3 Boundary Connection Technique for the Hybrid Method

The problem configuration is illustrated in Figure 18. The test model (Figure 18a) consists of an irregular free surface and an interface as a single layer crustal model. An artificial interface $\Gamma_{AB'}$ is introduced as a wavefield-connection boundary between the screen and BE methods. The whole model is divided into four subdomains, Ω_1, Ω_2 in the crust, and Ω_1', Ω_2' in the mantle. The left boundaries of Ω_1 and Ω_1' , and the right boundaries of Ω_2 and Ω_2' are assumed to extend to infinity. The wavefields in Ω_1 and Ω_1' are easy to calculate by the screen method. Its output field $u_0(\mathbf{r})$ on the connection interface $\Gamma_{AB'}$ will be used as the boundary condition when the BE method is used to calculate wave propagation in Ω_2 and Ω_2'. The output field is received along the next connection interface $\Gamma_{CD'}$, and will be used as the input to the screen method in the next propagation. In this way, a long distance propagation of the Lg phases through local complex waveguide structures with rough topographic features can be simulated by the hybrid scheme.

The total field $u(\mathbf{r})$ on the boundaries of Ω_2 and Ω_2' is composed of

$$u(\mathbf{r}) = \begin{cases} u_0(\mathbf{r}) + u_s(\mathbf{r}) & ,\mathbf{r} \in \Gamma_{AB'} \\ u_s(\mathbf{r}) & ,\mathbf{r} \notin \Gamma_{AB'} \end{cases} . \tag{37}$$

The boundary integral equation for fields on the boundaries of Ω_2 can be obtained from

$$C(\mathbf{r})u(\mathbf{r}) + \int_\Gamma u(\mathbf{r}')\frac{\partial G(\mathbf{r},\mathbf{r}')}{\partial n}d\mathbf{r}' = \int_\Gamma G(\mathbf{r},\mathbf{r}')\frac{\partial u(\mathbf{r}')}{\partial n}d\mathbf{r}'. \tag{38}$$

The surface Γ surrounding subdomain Ω_2 consists of the connection interface Γ_{AB}, the upper free surface Γ_1, the lower interface Γ_2, and the right boundary Γ_{CD}. Γ_{CD}, in computation, is assumed to be transparent and can be handled using an infinite element absorbing boundary technique (Fu and Wu, 1997). Therefore, the boundary integrals in eq. (38) can be decomposed into integrals over segments of the boundary. Considering eq. (37) and the free boundary condition on Γ_1 , the integral on the right of eq. (38) can be expressed as

$$\int_{\Gamma} G(\mathbf{r},\mathbf{r}')\frac{\partial}{\partial n}u(\mathbf{r}')d\mathbf{r}' = \int_{\Gamma_{AB}} G(\mathbf{r},\mathbf{r}')\frac{\partial}{\partial n}[u_0(\mathbf{r}')+u_s(\mathbf{r}')]d\mathbf{r}' + \int_{\Gamma_2} G(\mathbf{r},\mathbf{r}')\frac{\partial}{\partial n}u_s(\mathbf{r}')d\mathbf{r}'. \quad (39)$$

In order to solve $u_s(\mathbf{r})$ and $\partial u_s(\mathbf{r})/\partial n$ on Γ_2 , we must build the corresponding boundary integral equation in subdomain Ω_2' .

$$C(\mathbf{r})u_s(\mathbf{r}) + \int_{\Gamma'} u_s(\mathbf{r}')\frac{\partial}{\partial n}G(\mathbf{r},\mathbf{r}')d\mathbf{r}' = \int_{\Gamma'} G(\mathbf{r},\mathbf{r}')\frac{\partial}{\partial n}u_s(\mathbf{r}')d\mathbf{r}', \quad (40)$$

where $\Gamma' = \Gamma_{BB'} + \Gamma_2' + \Gamma_{DD'}$, and a sufficient long boundary $\Gamma_{BB'}$ is used with its end set into infinite element (Fu and Wu, 1997). The continuity of displacement and its normal gradient across interface Γ_{BD} is employed when eqs. (38) and (40) are combined to solve the problem. To solve eq. (38) using the boundary condition, the normal gradient of the field on $\Gamma_{AB'}$ must be calculated. It is easy to calculate $\partial u_0(\mathbf{r})/\partial n$ by the screen method. An alternative is to use the Rayleigh integral representation to eliminate the term $\partial u_0(\mathbf{r})/\partial n$. In addition, since there is no discontinuity across $\Gamma_{AB'}$, we can use the transparent boundary condition on $\Gamma_{AB'}$ for $u_s(\mathbf{r})$. By solving the joint boundary integral equations of Ω_2 and Ω_2' , we can obtain the wavefields $u_s(\mathbf{r})$ on Γ_1 and Γ_2 . The observation field along $\Gamma_{CD'}$ is calculated explicitly from the fields on the boundaries.

To test the validity of the connection technique, we present a comparison between the wavefield (Figure 18c) obtained using the BE method to directly calculate wave propagation from the source to the observation surface $\Gamma_{CD'}$ and the one (Figure 18d) by the hybrid method using the above connection scheme. In both cases, the source wavelet is the same, with the dominant frequency at 20 Hz. First, the screen method is used to compute the intermediate wavefield (Figure

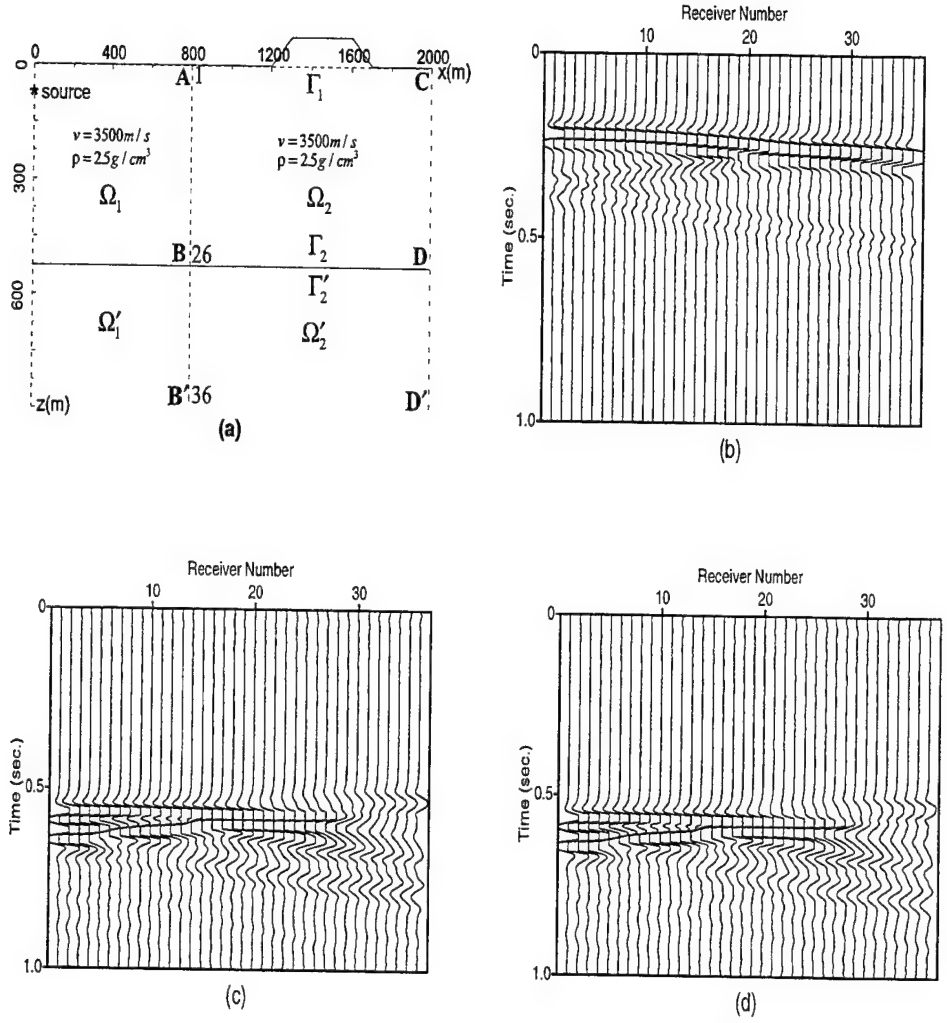

Figure 18: Test of wavefield connection. (a) Model geometry with receivers 1-36 located along $\Gamma_{AB'}$ and $\Gamma_{CD'}$ respectively. (b) The seismograms computed from the source to the connection boundary $\Gamma_{AB'}$. (c) The seismograms computed from the source directly to $\Gamma_{CD'}$. (d) The seismograms on $\Gamma_{CD'}$ computed using the wavefields on $\Gamma_{AB'}$ as the incident field. Comparison of wavefields (c) and (d) shows the validity of the connection technique.

18b) on $\Gamma_{AB'}$ as the incident field. Then, the BE method is used to calculate wave propagation from $\Gamma_{AB'}$ to $\Gamma_{CD'}$. The dominant arrivals for the incident field at $\Gamma_{AB'}$ consist of three sets of waves. The first arrival is the direct wave propagating from the source to receivers. The second is the reflected wave from the bottom interface, and the third is the reflected wave bounced back from the free surface. From the seismograms at $\Gamma_{CD'}$, more multiply reflected waves between the free surface and the interface can be clearly seen. The agreement between Figures 18c and 18d confirms the validity of the connection technique for the hybrid method.

4.4 Numerical Simulations on Surface Topography

In this section, we apply the hybrid method to regional wave propagation simulations. Figure 19 shows a laterally varying crust model. The first segment is a homogeneous waveguide 200 km in length, 32 km in thickness, with a SH wave velocity of 3.5 km/s over a half-space (4.5 km/s). The second segment is a complex waveguide consisting of two 6-km high, 20-km long mountain ridges centered at 240 km and 290 km. The last segment represents a 250 km horizontal waveguide of 32 km thickness with small-scale random heterogeneities. The random heterogeneities have an exponential correlation function with a correlation length 3 km in both horizontal and vertical directions, and a velocity perturbation 6%. The point source is located at 2 km depth. The receivers lie along both the free surface and vertical profiles at different distances with a 5 km spacing. Seismograms are computed in the frequency range 0 - 2 Hz.

First, the screen method is used to compute wave propagation from the source over 200 km to produce an initial wavefield on the first connection boundary Γ_{AB} . The synthetic seismograms are shown in Figure 20 with the receivers 1 - 7 above the Moho and 8 - 10 under the Moho. Multiple reflections within the crustal waveguide can be seen clearly from the seismograms. Then, the wavefields on Γ_{AB} are used as the incident fields, and the BE method is employed to calculate wave propagation for the next 120 km through the segment with the irregular topography. The

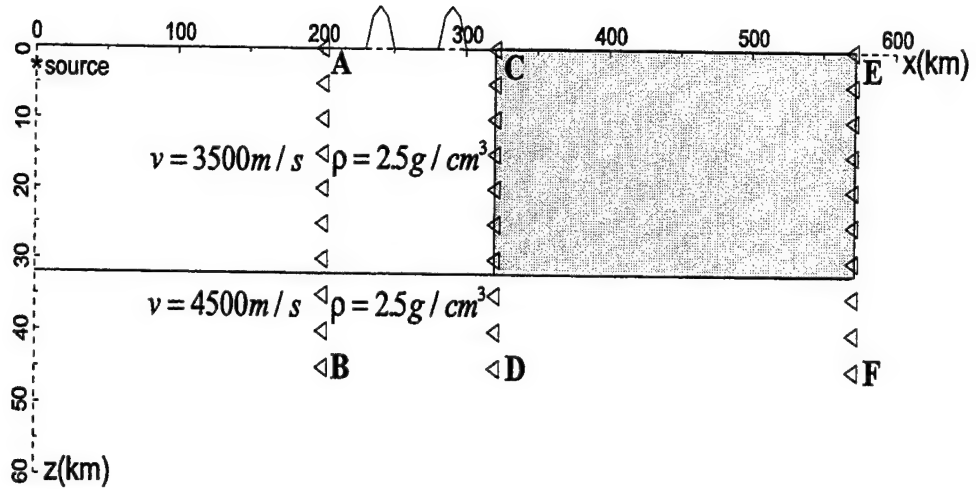

Figure 19: A laterally varying crustal model. The shadowed zone represents a random medium. The receivers are indicated by small triangles.

variable element dimension technique with 6 elements per wavelength is used in the program implementation to improve the computation speed. The synthetic seismograms shown in Figure 21 are recorded along both the free surface and the second connection boundary Γ_{CD} at 320 km. This result is compared to the seismogram in Figure 22, calculated using the hybrid method for the same segment of the model, but with a flat free-surface. Figure 23 shows the synthetic seismogram obtained using only the screen method to directly calculate wave propagation from the source to the connection boundary Γ_{CD} for the model with the flat free-surface. The agreement between Figures 22 and 17 shows the validity of the hybrid method for a long distance propagation.

The synthetic seismograms shown in Figure 21 are more complicated than those in Figure 22. The effects of the irregular topography on the guided waves can be seen from the comparison. The receivers located at or near irregular topographies have anomalous reflected signals due to the focusing/defocusing effects and the contamination by reverberations within these topographic structures (local site effects).

The most characteristic feature of the effects from the irregular topography

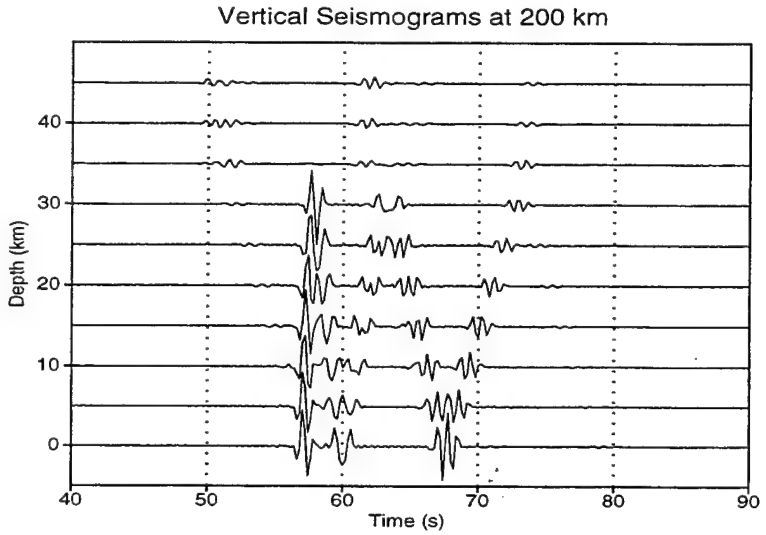

Figure 20: Synthetic seismograms along the first connection boundary at the distance of 200 km calculated by the screen method to produce an initial wavefield.

is the strong scattering by the topographic structures. This scattering has two consequences according to the propagation directions. One part is forescattering whose active time window is close to that of the wavetrain. Therefore, this tends to distort the wavetrain. Another part is backscattering that add new complexity to the waveguide wavetrains in Figure 21. In the surface seismograms, there are four groups of strong arrivals after the weak head waves: they are the direct, primary, doubly and triply reflected waves from the Moho. We see very little backscattering for the direct and primary reflected waves, but see clearly the backscattered waves for the doubly and triply reflected waves. Especially for the triply reflected waves, the backscatterings around the two mountain ridges at 240 km and 290 km are rather strong due to the favorable incident angles (steeper angles) in this case. From the vertical profile in Figure 21 (bottom panel) we see more mantle waves compared with Figure 22 (without topography). This is due to the leakage of crustal waves into the mantle by the mountain ridge scattering. At the same time, the multiply reflected crustal waves have been weakened, especially for the

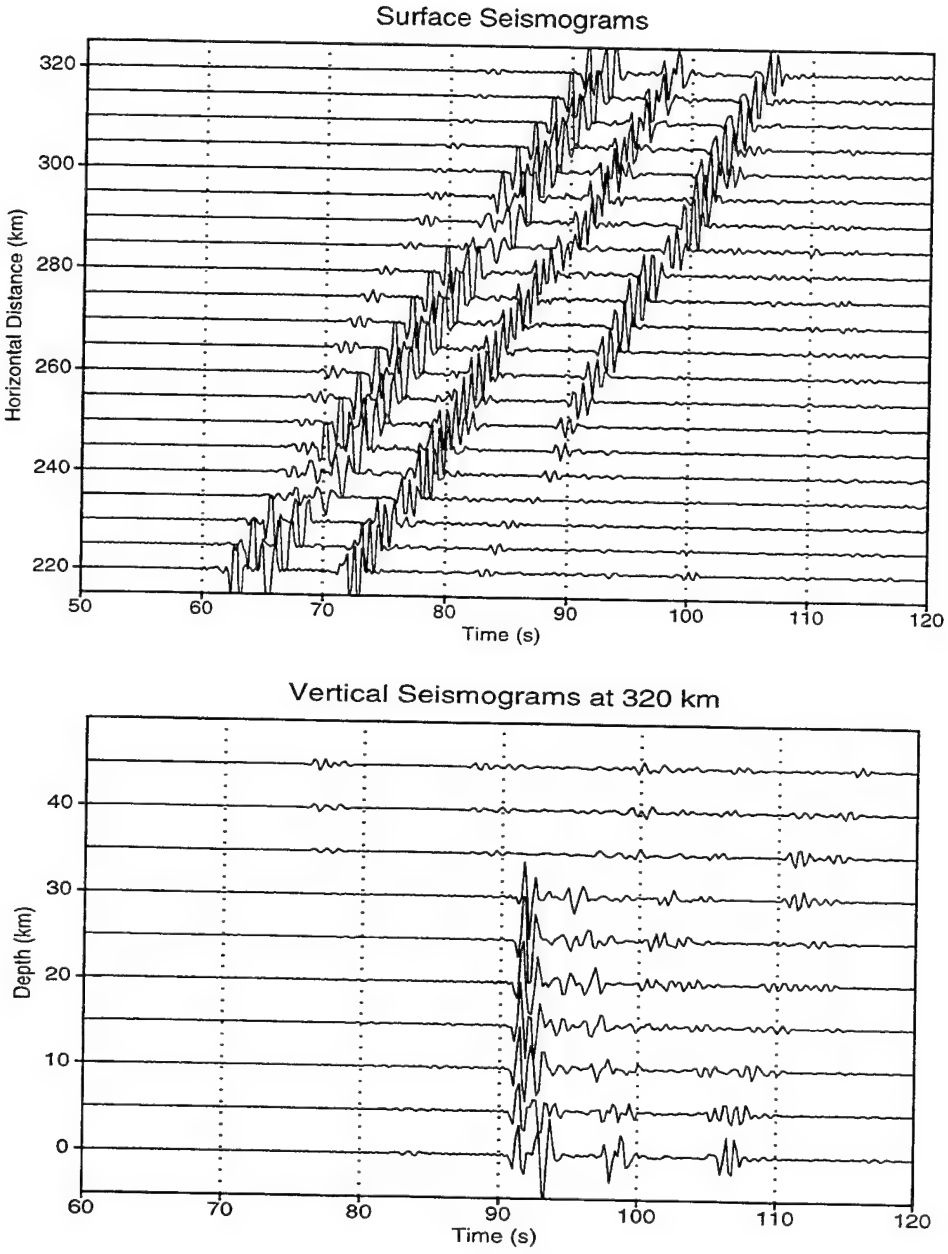

Figure 21: Synthetic seismograms calculated by the BE method using the wavefields in Figure 20 as the incident fields at 200 km. The receivers on the top panel are along the free surface with 5 km spacing, on the bottom, along a vertical profile (Γ_{CD}) at the distance of 320 km

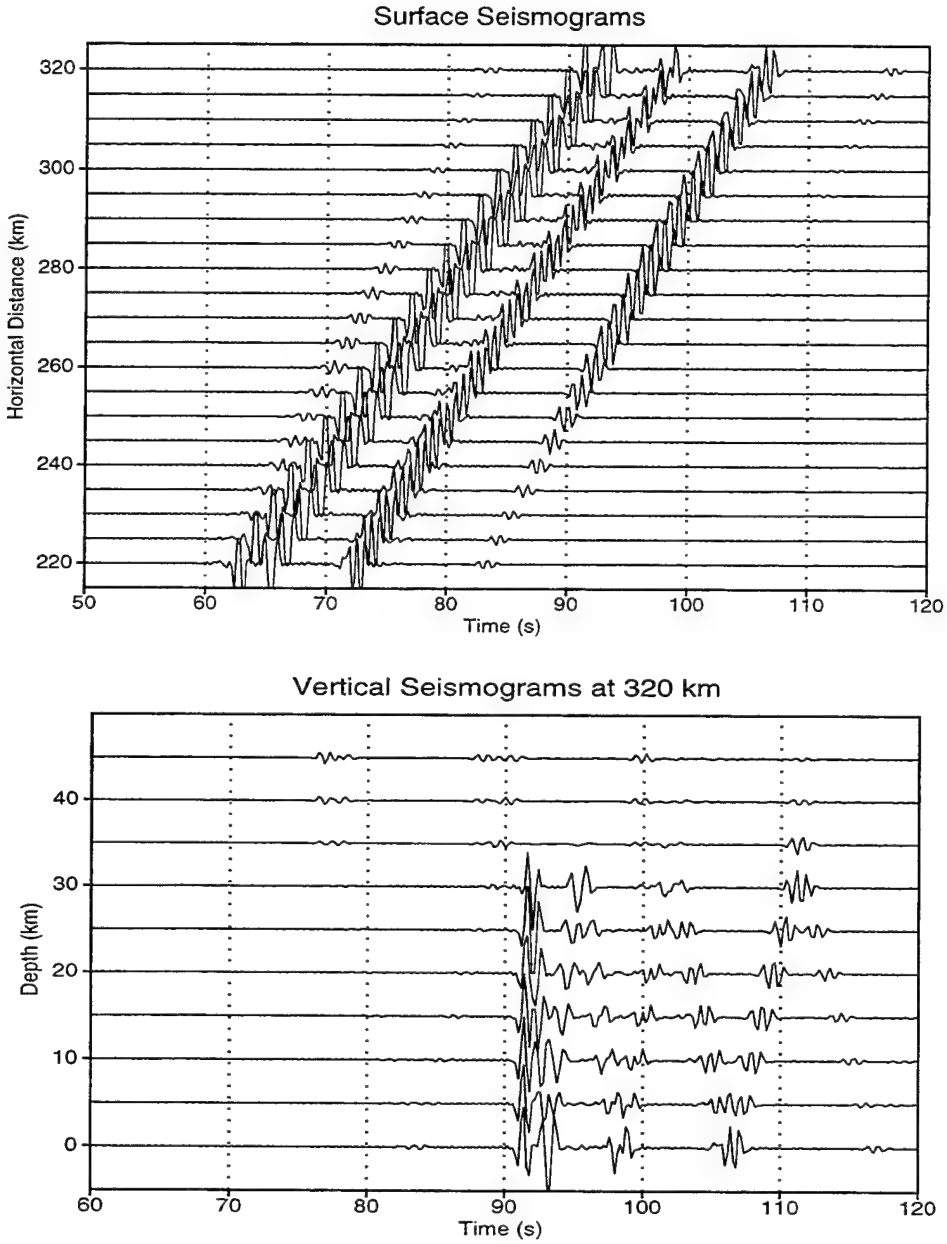

Figure 22: Same as Figure 21 except the free-surface is flat.

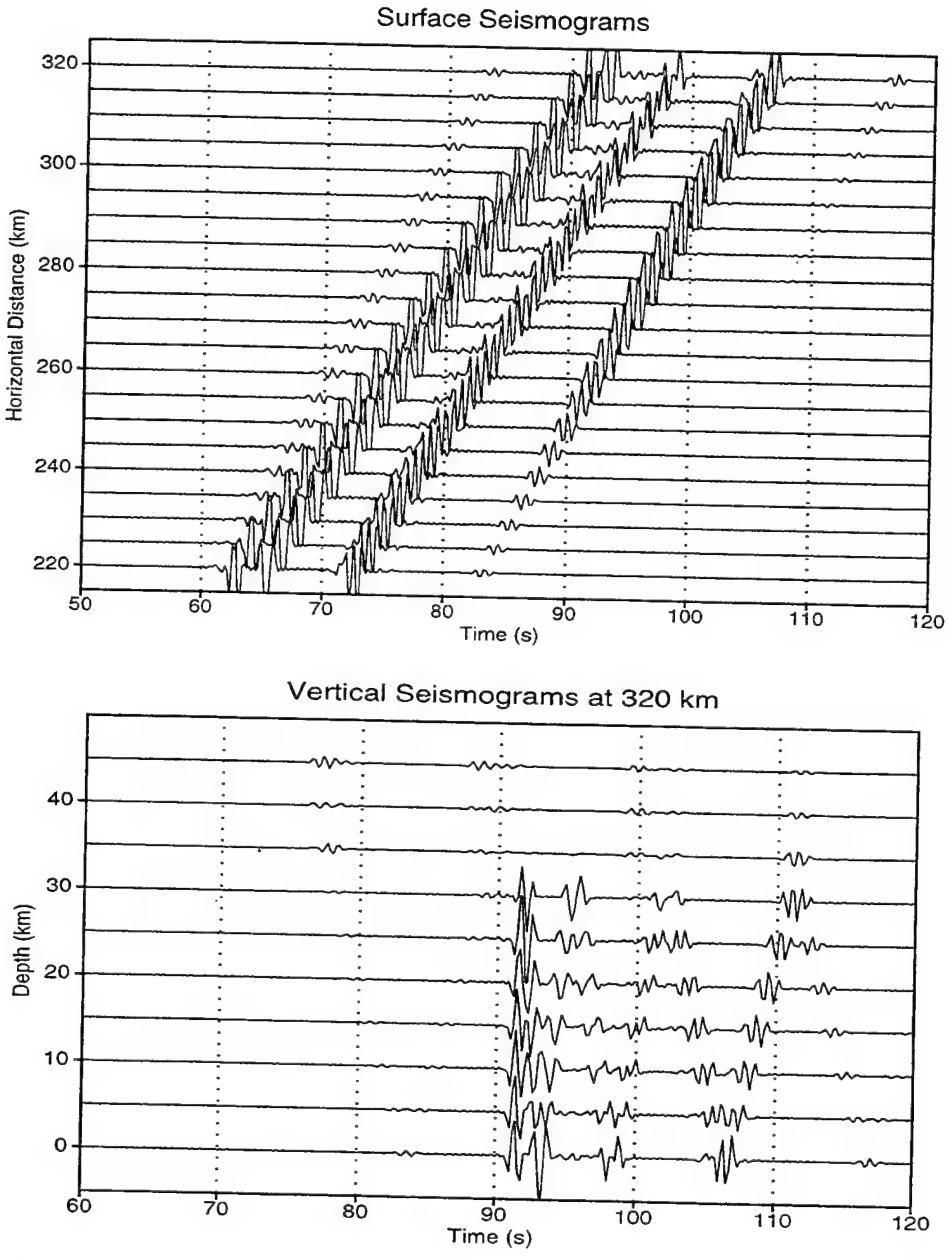

Figure 23: Same as Figure 22 except the screen method is used to directly calculate wave propagation from the source to the connection boundary Γ_{CD}.

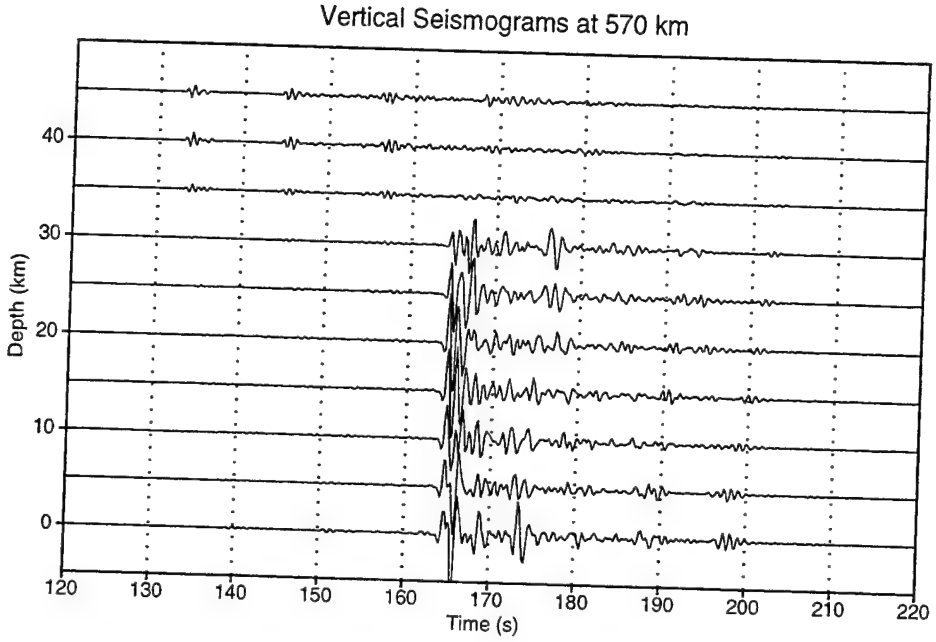

Figure 24: Synthetic seismograms along a vertical profile at the distance of 570 km calculated by the hybrid method. The wavefields in Figure 21 is used as the incident field and the propagation in the random medium is calculated by the screen method.

quadruply reflected waves (compared to Figure 22).

In summary, the scattering by local irregular topographies leads to anomalous near-receiver effects and tends to remove some energy from the guided waves, which causes decay of amplitude and waveform distortion. These scattered waves partly leak to the mantle and partly merge into the crustal guided waves. It can be expected that rough surface topography with scale length close to the dominant wavelength will be very efficient in attenuating Lg waves.

The synthetic seismograms shown in Figure 24 are obtained by using the wavefields on Γ_{CD} in Figure 21 as the input to the screen method and observing along the boundary Γ_{EF} at 570 km. The importance of small-scale random heterogeneities to seismic wave propagation is well known. The role of random heterogeneities in Lg wave propagation has been studied by Wu et al.(1996) using the

half-space generalized screen method, which shows that random heterogeneities drastically increase the leakage of waves to the mantle and the complexity of the waveforms.

5 Conclusions

Based on the newly developed half-space screen propagator method formulated by our group, hybrid methods have been proposed and tested for Lg wave simulation in highly complex crustal waveguides including surface topography for the two-dimensional SH case. We have derived the connection formulas for our hybrid schemes and their validity has been proved by numerical tests. Generalized screen method and both boundary integral equation and boundary element methods have been tested for the waveguide environment. The excellent agreement between seismograms for direct propagation and propagation using the connection formulas proves the correctness of the theory and the connection formulations. Numerical simulations on the influence of surface topography, sedimentary layers with rough bottom, and small-scale random heterogeneities demonstrate the feasibility of the methodology. It is also shown that rough surface topography and the rough bottom of sedimentary layers with scale close to the dominant wavelength can efficiently attenuate Lg waves. The next step is to develop the corresponding theory and algorithms for 2D P-SV and 3D elastic wave problems.

6 References

Aki, K., and Larner, K., 1970, Surface motion of a layered medium having an irregular interface due to incident plane SH waves: J. Geophys. Res., **75**, 934-954.

Aki, K., and P.G. Richards, 1980, Quantitative Seismology: Theory and Methods, Vol. 1 and 2, W.H. Freeman, New York.

Baumgardt, D. R., 1990, Investigation of teleseismic Lg blockage and scattering using regional arrays: Bull. Seis. Soc. Am., **80**, 2261-2281.

Benites, R., and Aki, K., 1989, Boundary integral-Gaussian beam method for seismic wave scattering: SH in two-dimensional media, J. Acoust. Soc. Am., **86**, 375-386.

Bouchon, M., 1985, A simple, complete numerical solution to the problem of diffraction of SH waves by an irregular interface: J. Acoust. Soc. Am., **77**, 1-5.

Bouchon, M., et al., 1985, Theoretical modeling of Lg wave attenuation, in The VELA Program; A Twenty-five Year Review of Basic Research.

Bouchon, M., Campillo, M. and Gaffet, S., 1989, A boundary integral equation-discrete wavenumber representation method to study wave propagation in multilayered media having irregular interfaces, Geophysics, **54**, 1134-1140.

Bouchon, M., Schultz, C. A., and Toksoz, M. N., 1996, Effect of three-dimensional topography on seismic motion: J. Geophys. Res., **101**, 5835-5846.

Campillo, M., and Bouchon, M., 1985, Synthetic SH-seismograms in a laterally varying medium by the discrete wavenumber method: Geophys. J. Roy. Astr. Soc., **83**, 307-317.

Campillo, M., 1990, Propagation and attenuation characteristics of the crustal phase Lg, Pure and Appl. Geophys., 132, 1-19.

Campillo, M., and Paul, A., 1992, Influence of lower crustal structure on the early coda of regional seismograms: J. Geophys. Res., **97**, 3405-3416.

Campillo, M., B. Feignier, M. Bouchon and N. Bethoux, 1993, Attenuation of

crustal waves across the Alpine range, J. Geophys. Res., 98, 1987-1996.

Chen, X. F., 1990, Seismogram synthesis for multi-layered media with irregular interfaces by the global generalized reflection/transmission matrices method - Part I. Theory of 2-D SH case: Bull. Seis. Soc. Am., **80**, 1694-1724.

Chen, X. F., 1995, Seismogram synthesis for multi-layered media with irregular interfaces by the global generalized reflection/transmission matrices method - Part II. Applications of 2-D SH case: Bull. Seis. Soc. Am., **85**, 1094-1106.

Chen, X. F., 1996, Seismogram synthesis for multi-layered media with irregular interfaces by the global generalized reflection/transmission matrices method - Part III. Theory of 2D P-SV case: Bull. Seis. Soc. Am., **86**, 389-405.

De Wolf, D.A., 1971, Electromagnetic reflection from an extended turbulent medium: cumulative forward-scatter single-backscatter approximation, IEEE trans. Ant. and Propag., AP-19, 254-262.

De Wolf, D.A., 1985, Renormalization of EM fields in application to large-angle scattering from randomly continuous media and sparse particle distributions, IEEE trans. Ant. and Propag., AP-33, 608-615.

Fornberg, B., 1987, The pseudospectral method: comparisons with finite differences for the elastic wave equation, Geophysics, **52**, 483-501.

Frankel, A., 1989, A review of numerical experiments on seismic wave scattering, in Scattering and Attenuation of Seismic Waves, II, edited by R.S. Wu and K. Aki, pp. 639-686, Birkhauser, Berlin.

Frankel, A. and R.W. Clayton, 1986, Finite difference simulations of seismic scattering: Implications for propagation of short-period seismic waves in the crust and models of crustal heterogeneity, J. Geophys. Res., 91, 6465-6489.

Fu, L. Y., and Mu, Y. G., 1994, Boundary element method for elastic wave forward modeling: Acta Geophys. Sinica, **37**, 521-529.

Fu, L. Y., 1996, 3-D boundary element seismic modeling in complex geology: 66th Ann. Internat. Mtg., Soc. Expl. Geophys., Expanded Abstracts, 1239-1242.

Fu, L. Y., and Wu, R. S., 1997, Infinite element-based absorbing boundary technique for elastic wave modeling: 67th Ann. Internat. Mtg., Soc. Expl. Geo-

phys., Expanded Abstracts, 1489-1492.

Gaffet, S., and Bouchon, M., 1989, Effects of two-dimensional topography using the discrete wavenumber-boundary integral equation method in P-SV cases, J. Acoust. Soc. Am., **85**, 2277-2283.

Gibson, Jr, R. L., and Campillo, M., 1994, Numerical simulation of high- and low-frequency Lg-wave propagation: Geophys. J. Int., **118**, 47-56.

Goldstein, P., C. Schultz, S. Larsen and L. Minner, 1996, Modeling of regional wave propagation phenomena in the middle east and north Africa and new analysis capabilities in SAC2000, Proceedings of the 18th Annual Seismic Research Smposium on Monitoring a Comprehensive Test Ban Treaty, 165-171, September 4-6, PL-TR-96-2153, ADA313692.

Gregersen, S., 1984, Lg wave propagation and crustal structure differences near Denmark and the North Sea: Geophys. J. Roy. Astr. Soc., **79**, 217-234.

Holliger, K. and A.R. Levander, 1992, A stochastic view of lower crustal fabric based on evidence from the Ivrea zone, Geophys. Res. Lett., 19, 1153-1156.

Horike, M., Uebayashi, H., and Takeuchi, H., 1990, Seismic response in three-dimensional sedimentary basin due to plane S wave incidence: J. Phys. Earth, **38**, 261-284.

Huang, L. J., and Wu, R. S., 1996, 3-D prestack depth migration with an acoustic pseudo-screen propagator. In: Mathematical Methods in Geophysical Imaging IV (ed. Hassanzadeh, S.), SPIE Proceedings Series, **2822**, 40-51.

Huang, L. J., and Fehler, M. C., 1998, Accuracy analysis of the split-step Fourier propagator: Implications for seismic modeling and migration: Bull. Seis. Soc. Am., **88**, 18-29.

Jih, R.S., 1996, Waveguide Effects of large-scale structural variation, anelastic attenuation, and random heterogeneity on SV Lg propagation: a finite-difference modeling study, Proceedings of the 18th Annual Seismic Research Symposium on Monitoring a Comprehensive Test Ban Treaty, 182-194, September 4-6, PL-TR-96-2153, ADA313692.

Kennett, B. L. N., Gregersen, S., Mykkeltveit, S., and Newmark, R., 1985, Map-

ping of crustal heterogeneity in the North Sea basin via the propagation of Lg-waves: Geophys. J. Roy. Astr. Soc., **83**, 299-306.

Kennet, B.L.N., 1989, Lg-wave propagation in heterogeneous media, Bull. Seismol. Soc. Am., 79, 860-872.

Kennet, B.L.N., 1990, Guided wave attenuation in laterally varying media, Geophys. J. Int., 100, 415-422.

Kim, J. and Papageorgiou, A. S., 1993, Discrete wave-number boundary-element method for 3-D scattering problems: J. Eng. Mech., **119**, 603-624.

Kosloff, D., D. Kessler, A. Quieroz, and E. Tessmer, 1990, Solution of the equations of Dynamic elasticity by a Chebychev spectral method, Geophysics, 55, 734-748.

Levander, A.. and K. Holliger, 1992, Small-scale heterogeneity and large-scale velocity structure of the continental crust, J. Geophys. Res., 97, 7897-8804.

Lee, J. J., and Langston, C. A., 1983, Wave propagation in a three-dimensional circular basin: Bull. Seis. Soc. Am., **61**, 1637-1653.

Liu, Y. B., and Wu, R. S., A comparison between phase screen, finite difference, and eigenfunction expansion calculations for scalar waves in inhomogeneous media: Bull. Seis. Soc. Am., **84**, 1154-1168.

Martin, J. M., and Flatte, S. M., 1988, Intensity images and statistics from numerical simulation of wave propagation in 2-D random media: Appl. Opt., **17**, 2111-2126.

Maupin V., 1989, Numerical modeling of Lg wave propagation across the North Sea central graben, Geophys. J. Int., 99, 273-283.

Moczo, P., Bystricky, E., Kristek, J., Carcione, J. M., and Bouchon, M., 1997, Hybrid modeling of P-SV seismic motion at inhomogeneous viscoelastic topographic structures: Bull. Seis. Soc. Am., **87**, 1305-1323.

Morse, P.M., and H. Feshbach, 1953, Methods of Theoretical Physics, chapter 7, McGraw-Hill Book Comp., New York.

Papageorgiou, A. S., and Kim, J., 1993, Propagation and amplification of seismic waves in 2-D valleys excited by obliquely incident P- and S- waves, Earthquake

Eng. And Struct. Dyn., **22**, 167-182.

Sanchez-Sesma, F.J., Perez-Roch, L. E., and Chavez-Perez, S., 1989, Diffraction of elastic waves by three-dimensional surface irregularities, Part II: Bull. Seis. Soc. Am., **79**, 101-112.

Sanchez-Sesma, F.J., and Campillo, M., 1991, Diffraction of P, SV and Rayleigh waves by topographic features: a boundary integral formulation, Bull. Seis. Soc. Am., **81**, 2234-2253.

Sanchez-Sesma, F.J., and Campillo, M., 1993, Topographic effects for incident P, SV and Rayleigh waves, Tectonophysics, **218**, 113-125.

Schatzman, J.C., 1996, A pseudo-spectral scheme for viscoelastic seismic modeling, Proceedings of the 18th Annual Seismic Research Smposium on Monitoring a Comprehensive Test Ban Treaty, 261-270, September 4-6, PL-TR-96-2153, ADA313692.

Sei, A., 1993, Computational cost of finite-difference elastic waves modeling: 63th Ann. Internat. Mtg., Soc. Expl. Geophys., Expanded Abstracts, 1065-1068.

Stoffa, P. L., Fokkema, J. T., Freire, R. M. D., and Kessinger, W. P., 1990, Split-step Fourier migration: Geophysics, **55**, 410-421.

Trifunac, M.D., 1971, Surface motion of a semi-cylindrical alluvial valley for incident plane SH waves, Bull. Seism. Soc. Am. **61**, 1755-1770.

Trifunac, M.D., 1973, Scattering of plane SH waves by a semi-cylindrical canyon, Earthquake Eng. Struct. Dyn. **1**, 267-281.

Wetmiller, R. J., 1974, Crustal structure of Baffin Bay from earthquake generated Lg phases: Can. J. Earth Sci. **11**, 123-130.

Wu, R. S., 1994, Wide-angle elastic wave one-way propagation in heterogeneous media and an elastic wave complex-screen method: J. Geophys. Res., **99**, 751-766.

Wu, R.S., Z. Xu, and X.P. Li, 1994, Heterogeneity spectrum and scale-anisotropy in the upper crust revealed by the German continental deep-drilling (KTB) holes, Geophys. Res. Lett., 21, 911-914.

Wu, R. S., 1996, Synthetic seismogram in heterogeneous media by one-return ap-

proximation: Pure and Applied Geophys., **148**, 155-173.

Wu, R. S., and Xie, X. B., 1994, Multi-screen backpropagator for fast 3D elastic prestack migration. In: Mathematical Methods in Geophysical Imaging II (ed. Hassanzadeh, S.), SPIE Proceedings Series, **2301**, 181-193.

Wu, R. S., and Huang, L. J., 1995, Reflected wave modeling in heterogeneous acoustic media using the De Wolf approximation. In: Mathematical Methods in Geophysical Imaging III (ed. Hassanzadeh, S.), SPIE Proceedings Series, **2571**, 176-186.

Wu, R. S., Lay, T., and Chen, X. F., 1996, Modeling the effects of surface topography on Lg wave propagation by a hybrid method: Proceedings of the 18th Annual Seismic Research Symposium, 281-290, PL-TR-96-2153, ADA313692.

Wu, R. S., Jin, S., and Xie, X. B., 1996, Synthetic seismograms in heterogeneous crustal waveguides using screen propagators: Proceedings of the 18th Annual Seismic Research Symposium, 291-300, PL-TR-96-2153, ADA313692.

Wu, R.S., S. Jin, X.B. Xie, and T. Lay, 1997, Verification and applications of GSP (Generalized screen propagators) method for regional wave propagation, Proceeding of 19th Annual Seismic Research Symposium on Monitoring a Comprehensive Test Ban Treaty, 552-561.

Wu, R.S., S. Jin and X.B. Xie, 1998, Seismic wave propagation and scattering in heterogeneous crustal waveguides using screen propagators: I SH-waves, submitted to J. Geophys. Res..

Xie, X. B. and Lay, T., 1994, The excitation of explosion Lg, a finite-difference investigation: Bull. Seis. Soc. Am., **84**, 324-3428.

Xie, X.B. and R.S. Wu, 1995, A complex-screen method for modeling elastic wave reflections, Expanded Abstracts, SEG 65th Annual Meeting, 1269-1272.

Xie, X.B. and R.S. Wu, 1996, 3D elastic wave modeling using the complex screen method, Expanded Abstracts, SEG 66th Annual Meeting, 1247-1250.

Zhang, T., and Lay, T., 1994, Effects of crustal structure under the Barents and Kara seas on short-period regional wave propagation for Novaya Zemlya explosions: Empirical relations: Bull. Seis. Soc. Am., **84**, 1132-1147.

THOMAS AHRENS
SEISMOLOGICAL LABORATORY 252-21
CALIFORNIA INST. OF TECHNOLOGY
PASADENA, CA 91125

AIR FORCE RESEARCH LABORATORY
ATTN: VSOP
29 RANDOLPH ROAD
HANSCOM AFB, MA 01731-3010 (2 COPIES)

AIR FORCE RESEARCH LABORATORY
ATTN: RESEARCH LIBRARY/TL
5 WRIGHT STREET
HANSCOM AFB, MA 01731-3004

AIR FORCE RESEARCH LABORATORY
ATTN: AFRL/SUL
3550 ABERDEEN AVE SE
KIRTLAND AFB, NM 87117-5776 (2 COPIES)

RALPH ALEWINE
NTPO
1901 N. MOORE STREET, SUITE 609
ARLINGTON, VA 22209

MUAWIA BARAZANGI
INSTOC
3126 SNEE HALL
CORNELL UNIVERSITY
ITHACA, NY 14853

DOUGLAS BAUMGARDT
ENSCO INC.
5400 PORT ROYAL ROAD
SPRINGFIELD, VA 22151

THERON J. BENNETT
MAXWELL TECHNOLOGIES
11800 SUNRISE VALLEY
SUITE 1212
RESTON, VA 22091

WILLIAM BENSON
NAS/COS
ROOM HA372
2001 WISCONSIN AVE. NW
WASHINGTON DC 20007

JONATHAN BERGER
UNIV. OF CALIFORNIA, SAN DIEGO
SCRIPPS INST. OF OCEANOGRAPHY IGPP, 0225
9500 GILMAN DRIVE
LA JOLLA, CA 92093-0225

ROBERT BLANDFORD
AFTAC
1300 N. 17TH STREET
SUITE 1450
ARLINGTON, VA 22209-2308

LESLIE A. CASEY
DEPT. OF ENERGY/NN-20
1000 INDEPENDENCE AVE. SW
WASHINGTON DC 20585-0420

CENTER FOR MONITORING RESEARCH
ATTN: LIBRARIAN
1300 N. 17th STREET, SUITE 1450
ARLINGTON, VA 22209

FRANCESCA CHAVEZ
LOS ALAMOS NATIONAL LAB
P.O. BOX 1663, MS-D460
LOS ALAMOS, NM 87545 (5 COPIES)

ANTON DAINTY
DTRA/PMA
45045 AVIATION DRIVE
DULLESVA 20166-7517

CATHERINE DE GROOT-HEDLIN
UNIV. OF CALIFORNIA, SAN DIEGO
IGPP
8604 LA JOLLA SHORES DRIVE
SAN DIEGO, CA 92093

DIANE DOSER
DEPT. OF GEOLOGICAL SCIENCES
THE UNIVERSITY OF TEXAS AT EL PASO
EL PASO, TX 79968

DTIC
8725 JOHN J. KINGMAN ROAD
FT BELVOIR, VA 22060-6218 (2 COPIES)

MARK D. FISK
MISSION RESEARCH CORPORATION
735 STATE STREET
P.O. DRAWER 719
SANTA BARBARA, CA 93102-0719

HENRY GRAY
SMU STATISTICS DEPARTMENT
P.O. BOX 750302
DALLAS, TX 75275-0302

I. N. GUPTA
MULTIMAX, INC.
1441 MCCORMICK DRIVE
LARGO, MD 20774

DAVID HARKRIDER
BOSTON COLLEGE
24 MARTHA'S PT. RD.
CONCORD, MA 01742

THOMAS HEARN
NEW MEXICO STATE UNIVERSITY
DEPARTMENT OF PHYSICS
LAS CRUCES, NM 88003

MICHAEL HEDLIN
UNIVERSITY OF CALIFORNIA, SAN DIEGO
SCRIPPS INST. OF OCEANOGRAPHY
9500 GILMAN DRIVE
LA JOLLA, CA 92093-0225

DONALD HELMBERGER
CALIFORNIA INST. OF TECHNOLOGY
DIV. OF GEOL. & PLANETARY SCIENCES
SEISMOLOGICAL LABORATORY
PASADENA, CA 91125

EUGENE HERRIN
SOUTHERN METHODIST UNIVERSITY
DEPT. OF GEOLOGICAL SCIENCES
DALLAS, TX 75275-0395

ROBERT HERRMANN
ST. LOUIS UNIVERSITY
DEPT. OF EARTH & ATMOS. SCIENCES
3507 LACLEDE AVENUE
ST. LOUIS, MO 63103

VINDELL HSU
HQ/AFTAC/TTR
1030 S. HIGHWAY A1A
PATRICK AFB, FL 32925-3002

RONG-SONG JIH
DTRA/PMA
45045 AVIATION DRIVE
DULLES, VA 20166-7517

THOMAS JORDAN
MASS. INST. OF TECHNOLOGY
BLDG 54-918
CAMBRIDGE, MA 02139

LAWRENCE LIVERMORE NAT'L LAB
ATTN: TECHNICAL STAFF (PLS ROUTE)
PO BOX 808, MS L-208
LIVERMORE, CA 94551

LAWRENCE LIVERMORE NAT'L LAB
ATTN: TECHNICAL STAFF (PLS ROUTE)
PO BOX 808, MS L-205
LIVERMORE, CA 94551

LAWRENCE LIVERMORE NAT'L LAB
ATTN: TECHNICAL STAFF (PLS ROUTE)
PO BOX 808, MS L-200
LIVERMORE, CA 94551

THORNE LAY
UNIV. OF CALIFORNIA, SANTA CRUZ
EARTH SCIENCES DEPARTMENT
EARTH & MARINE SCIENCE BUILDING
SANTA CRUZ, CA 95064

ANATOLI L. LEVSHIN
DEPARTMENT OF PHYSICS
UNIVERSITY OF COLORADO
CAMPUS BOX 390
BOULDER, CO 80309-0309

JAMES LEWKOWICZ
WESTON GEOPHYSICAL CORP.
325 WEST MAIN STREET
NORTHBORO, MA 01532

LOS ALAMOS NATIONAL LABORATORY
ATTN: TECHNICAL STAFF (PLS ROUTE)
PO BOX 1663, MS D460
LOS ALAMOS, NM 87545

LOS ALAMOS NATIONAL LABORATORY
ATTN: TECHNICAL STAFF (PLS ROUTE)
PO BOX 1663, MS F665
LOS ALAMOS, NM 87545

LOS ALAMOS NATIONAL LABORATORY
ATTN: TECHNICAL STAFF (PLS ROUTE)
PO BOX 1663, MS C335
LOS ALAMOS, NM 87545

KEITH MCLAUGHLIN
CENTER FOR MONITORING RESEARCH
SAIC
1300 N. 17TH STREET, SUITE 1450
ARLINGTON, VA 22209

RICHARD MORROW
USACDA/IVI
320 21ST STREET, N.W.
WASHINGTON DC 20451

JAMES NI
NEW MEXICO STATE UNIVERSITY
DEPARTMENT OF PHYSICS
LAS CRUCES, NM 88003

OFFICE OF THE SECRETARY OF DEFENSE
DDR&E
WASHINGTON DC 20330

PACIFIC NORTHWEST NAT'L LAB
ATTN: TECHNICAL STAFF (PLS ROUTE)
PO BOX 999, MS K5-12
RICHLAND, WA 99352

KEITH PRIESTLEY
DEPARTMENT OF EARTH SCIENCES
UNIVERSITY OF CAMBRIDGE
MADINGLEY RISE, MADINGLEY ROAD
CAMBRIDGE, CB3 OEZ UK

DELAINE REITER
WESTON GEOPHYSICAL CORP.
73 STANDISH ROAD
WATERTOWN, MA 0472

MICHAEL RITZWOLLER
DEPARTMENT OF PHYSICS
UNIVERSITY OF COLORADO
CAMPUS BOX 390
BOULDER, CO 80309-0309

CHANDAN SAIKIA
WOOODWARD-CLYDE FED. SERVICES
566 EL DORADO ST., SUITE 100
PASADENA, CA 91101-2560

GARY MCCARTOR
SOUTHERN METHODIST UNIVERSITY
DEPARTMENT OF PHYSICS
DALLAS, TX 75275-0395

BRIAN MITCHELL
DEPARTMENT OF EARTH & ATMOSPHERIC SCIENCES
ST. LOUIS UNIVERSITY
3507 LACLEDE AVENUE
ST. LOUIS, MO 63103

JOHN MURPHY
MAXWELL TECHNOLOGIES
11800 SUNRISE VALLEY DRIVE
SUITE 1212
RESTON, VA 22091

ROBERT NORTH
CENTER FOR MONITORING RESEARCH
1300 N. 17th STREET, SUITE 1450
ARLINGTON, VA 22209

JOHN ORCUTT
INST. OF GEOPH. & PLANETARY PHYSICS
UNIV. OF CALIFORNIA, SAN DIEGO
LA JOLLA, CA 92093

FRANK PILOTTE
HQ AFTAC/TT
1030 S. HIGHWAY A1A
PATRICK AFB, FL 32925-3002

JAY PULLI
BBN SYSTEMS AND TECHNOLOGIES, INC.
1300 NORTH 17TH STREET
ROSSLYN, VA 22209

PAUL RICHARDS
COLUMBIA UNIVERSITY
LAMONT-DOHERTY EARTH OBSERV.
PALISADES, NY 10964

DAVID RUSSELL
HQ AFTAC/TTR
1030 SOUTH HIGHWAY A1A
PATRICK AFB, FL 32925-3002

SANDIA NATIONAL LABORATORY
ATTN: TECHNICAL STAFF (PLS ROUTE)
DEPT. 9311
MS 1159, PO BOX 5800
ALBUQUERQUE, NM 87185-1159

SANDIA NATIONAL LABORATORY
ATTN: TECHNICAL STAFF (PLS ROUTE)
DEPT. 5736
MS 0655, PO BOX 5800
ALBUQUERQUE, NM 87185-0655

AVI SHAPIRA
SEISMOLOGY DIVISION
IPRG
P.O.B. 2286 NOLON 58122 ISRAEL

MATTHEW SIBOL
ENSCO, INC.
445 PINEDA CT.
MELBOURNE, FL 32940

JEFFRY STEVENS
MAXWELL TECHNOLOGIES
8888 BALBOA AVE.
SAN DIEGO, CA 92123-1506

TACTEC
BATTELLE MEMORIAL INSTITUTE
505 KING AVENUE
COLUMBUS, OH 43201 (FINAL REPORT)

LAWRENCE TURNBULL
ACIS
DCI/ACIS
WASHINGTON DC 20505

FRANK VERNON
UNIV. OF CALIFORNIA, SAN DIEGO
SCRIPPS INST. OF OCEANOGRAPHY
9500 GILMAN DRIVE
LA JOLLA, CA 92093-0225

RU SHAN WU
UNIV. OF CALIFORNIA, SANTA CRUZ
EARTH SCIENCES DEPT.
1156 HIGH STREET
SANTA CRUZ, CA 95064

JAMES E. ZOLLWEG
BOISE STATE UNIVERSITY
GEOSCIENCES DEPT.
1910 UNIVERSITY DRIVE
BOISE, ID 83725

SANDIA NATIONAL LABORATORY
ATTN: TECHNICAL STAFF (PLS ROUTE)
DEPT. 5704
MS 0655, PO BOX 5800
ALBUQUERQUE, NM 87185-0655

THOMAS SERENO JR.
SAIC
10260 CAMPUS POINT DRIVE
SAN DIEGO, CA 92121

ROBERT SHUMWAY
410 MRAK HALL
DIVISION OF STATISTICS
UNIVERSITY OF CALIFORNIA
DAVIS, CA 95616-8671

DAVID SIMPSON
IRIS
1200 NEW YORK AVE., NW
SUITE 800
WASHINGTON DC 20005

BRIAN SULLIVAN
BOSTON COLLEGE
INSITUTE FOR SPACE RESEARCH
140 COMMONWEALTH AVENUE
CHESTNUT HILL, MA 02167

NAFI TOKSOZ
EARTH RESOURCES LABORATORY
M.I.T.
42 CARLTON STREET, E34-440
CAMBRIDGE, MA 02142

GREG VAN DER VINK
IRIS
1200 NEW YORK AVE., NW
SUITE 800
WASHINGTON DC 20005

TERRY WALLACE
UNIVERSITY OF ARIZONA
DEPARTMENT OF GEOSCIENCES
BUILDING #77
TUCSON, AZ 85721

JIAKANG XIE
COLUMBIA UNIVERSITY
LAMONT DOHERTY EARTH OBSERV.
ROUTE 9W
PALISADES, NY 10964